bioRxiv preprint doi: https://doi.org/10.1101/2021.05.18.444618; this version posted May 19, 2021. The copyright holder for this preprint (which was not certified by peer review) is the author/funder, who has granted bioRxiv a license to display the preprint in perpetuity. It is made available under aCC-BY 4.0 International license.

Modulation of fracture healing by the transient accumulation of senescent cells

Abbreviated Title: Senescence in fracture healing

Authors: Dominik Saul, M.D.[1,2,3], David G. Monroe, Ph.D.[1,2,5], Jennifer L. Rowsey, B.S.[1,2], Robyn L. Kosinsky, Ph.D.[4], Stephanie J. Vos, B.S. [1,2], Madison L. Doolittle, Ph.D.[1,2], Joshua N. Farr, Ph.D.[1,2,5*] and Sundeep Khosla, M.D.[1,2,5*]

Affiliations: [1]Division of Endocrinology, Mayo Clinic, Rochester, MN 55905, USA; [2]Robert and Arlene Kogod Center on Aging, Mayo Clinic, Rochester, MN 55905, USA; [3]Department of Trauma, Orthopedics and Reconstructive Surgery, Georg-August-University of Goettingen, Germany, [4]Division of Gastroenterology and Hepatology, Mayo Clinic, Rochester, MN 55905, USA; [5]Division of Physiology and Biomedical Engineering; Mayo Clinic College of Medicine, Mayo Clinic, Rochester MN, 55905, USA.

Funding: This work was supported by the German Research Foundation (DFG, 413501650) (D.S.), National Institutes of Health (NIH) grants P01 AG062413 (S.K., J.N.F.), R21 AG065868 (S.K., J.N.F), K01 AR070241 (J.N.F.), R01 AG063707 (D.G.M.), and Mildred Scheel postdoc fellowship by the German Cancer Aid (R.L.K.).

Emails:

- Dominik Saul: saul.dominik@mayo.edu; ORCiD: 0000-0002-0673-3710
- David G. Monroe: monroe.david@mayo.edu; ORCiD: 0000-0002-4818-0114
- Jennifer L. Rowsey: rowsey.jennifer@mayo.edu
- Robyn L. Kosinsky: kosinsky.robynlaura@mayo.edu; ORCiD: 0000-0003-2869-7762
- Stephanie J. Vos: vos.stephanie@mayo.edu
- Madison L. Doolittle: doolittle.madison@mayo.edu; ORCiD: 0000-0003-0912-0095
- Joshua N. Farr: farr.joshua@mayo.edu; ORCiD: 0000-0002-3179-6414
- Sundeep Khosla: khosla.sundeep@mayo.edu; ORCiD: 0000-0002-2936-4372

***Corresponding authors:**

*Joshua N. Farr, Ph.D., Guggenheim 7, Mayo Clinic College of Medicine, 200 First Street SW, Rochester, MN 55905; Tel. +1-507-538-0085; Fax. +1-507-284-9111; Email: farr.joshua@mayo.edu

*Sundeep Khosla, M.D., Guggenheim 7, Mayo Clinic College of Medicine, 200 First Street SW, Rochester, MN 55905; Tel: +507-255-6663; Email: khosla.sundeep@mayo.edu

Key Words: bone, bone healing, fracture, senescence, callus

Supplementary Material: This manuscript contains Supplementary Information, Figures, and Tables

Disclosures: The authors have declared that no conflict of interest exists.

bioRxiv preprint doi: https://doi.org/10.1101/2021.05.18.444618; this version posted May 19, 2021. The copyright holder for this preprint (which was not certified by peer review) is the author/funder, who has granted bioRxiv a license to display the preprint in perpetuity. It is made available under aCC-BY 4.0 International license.

Abstract

Senescent cells have detrimental effects across tissues with aging but may have beneficial effects on tissue repair, specifically on skin wound healing. However, the potential role of senescent cells in fracture healing has not been defined. Here, we performed an *in silico* analysis of public mRNAseq data and found that senescence and senescence-associated secretory phenotype (SASP) markers increased during fracture healing. We next directly established that the expression of senescence biomarkers increased markedly during murine fracture healing. We also identified a subset of cells in the fracture callus that displayed hallmarks of senescence, including distension of satellite heterochromatin and telomeric DNA damage. Then, using a genetic mouse model ($p16^{LUC}$) containing a $p16^{Ink4a}$-driven luciferase reporter, we demonstrated transient *in vivo* senescent cell accumulation during callus formation. Finally, we intermittently treated young adult mice following fracture with drugs that selectively eliminate senescent cells ("senolytics", Dasatinib plus Quercetin), and showed that this regimen both decreased senescence and SASP markers in the fracture callus and significantly accelerated the time course of fracture healing. Our findings thus demonstrate that senescent cells accumulate transiently in the murine fracture callus and, in contrast to the skin, their clearance does not impair but rather may improve fracture healing.

bioRxiv preprint doi: https://doi.org/10.1101/2021.05.18.444618; this version posted May 19, 2021. The copyright holder for this preprint (which was not certified by peer review) is the author/funder, who has granted bioRxiv a license to display the preprint in perpetuity. It is made available under aCC-BY 4.0 International license.

Introduction

The worldwide burden of fractures is growing. One reason for this major public health problem is population aging, which is associated with progressive physiological decline, leading to an increased risk for many chronic diseases *(1)*. Hallmarks of aging that drive this deterioration include genomic instability, telomere attrition, epigenetic alterations, loss of proteostasis, deregulated nutrient sensing, mitochondrial dysfunction, stem cell exhaustion, altered intercellular communication, and cellular senescence *(2)*. Recently, cellular senescence has emerged as a promising therapeutic target to prevent aging of multiple tissues, including the musculoskeletal system *(3–7,1,8)*. Because the "geroscience hypothesis" postulates that targeting fundamental mechanisms of aging, such as cellular senescence, can delay the onset of age-associated diseases as a group, a better understanding of the beneficial versus detrimental roles of senescent cells throughout the lifespan in various physiological contexts, such as fracture healing, is of considerable importance *(1)*.

Similar to other tissues, senescent cells accumulate within the aged bone microenvironment and are causal in the pathogenesis of age-related bone loss *(9,4,6)*. One key feature of the cellular senescence program is activation of the cyclin-dependent kinase inhibitors (CDKIs), $p16^{Ink4a}$ (*Cdkn2a*) and $p21^{Cip1}$ (*Cdkn1a*), paralleled by apoptosis resistance via upregulation of senescent cell anti-apoptotic pathways *(10)*. In the murine bone marrow, predominantly $p16^{Ink4a}$ and to a lesser extent $p21^{Cip1}$ have been linked to aging in diverse cellular populations such as B- and T-cells, myeloid cells, osteoprogenitors, osteoblasts, and osteocytes *(9)*. Along with increased CDKI expression, senescent cells develop a senescence-associated secretory phenotype (SASP), consisting of pro-inflammatory cytokines, chemokines, and extracellular matrix degrading proteins that can drive tissue dysfunction via paracrine and systemic intercellular signaling, and spread cellular senescence through a so-called "bystander effect" *(11–13)*. These detrimental effects can be alleviated by clearing senescent cells either genetically or by administration of senolytics – drugs that selectively kill senescent cells. For example, intermittent delivery of the senolytic cocktail, Dasatinib (D, a tyrosine kinase inhibitor) plus Quercetin (Q, a natural flavonoid) has been shown to eliminate senescent cells in old mice and in humans and, in preclinical studies, slows the onset of aging by preventing multiple co-morbidities to thereby extend healthspan *(6,14,9)*. These findings are now being translated into humans, and D+Q is currently undergoing human trials for safety and efficacy to prevent age-related skeletal deterioration (NCT04313634).

bioRxiv preprint doi: https://doi.org/10.1101/2021.05.18.444618; this version posted May 19, 2021. The copyright holder for this preprint (which was not certified by peer review) is the author/funder, who has granted bioRxiv a license to display the preprint in perpetuity. It is made available under aCC-BY 4.0 International license.

In youth, beneficial physiological functions of senescent cells and their SASP have been suggested in skin wound healing, as senescent fibroblasts and endothelial cells are recruited to sites of injury where they release SASP factors that, in turn, attract various cell populations (e.g., immune cells) to accelerate skin wound healing. Indeed, after an early appearance in the healing skin wound, senescent cells induce myofibroblast differentiation and secrete PDGF-AA, a crucial factor necessary for proper wound healing *(15)*. However, the dynamics of skin wound healing do not directly translate to the various bone healing repair phases (i.e., inflammatory, soft callus, hard callus and remodeling phase). Indeed, bone has the exclusive ability to form scar-free tissue *de novo*, although this process is slower than the typical wound healing process *(16)*. Importantly, manipulation at each stage can change the course of natural fracture healing events, which has been demonstrated by our group previously *(17,18)*. Whether senescent cells appear in the healing skeleton as they do in skin wound healing or how these cells modulate fracture repair is not known. Indeed, to the extent that senolytic drugs progress to clinical use, particularly in patients with osteoporosis, it is critical to understand whether senescent cells play a similar, beneficial role in bone fracture healing as appears to be the case in the skin*(15)*. For example, if clearance of senescent cells impairs the time course or final outcome of the fracture healing process, that would clearly adversely impact the potential use of senolytic therapies in patients with osteoporosis.

In this context, the aims of this study were to characterize the potential appearance of senescent cells during fracture healing and establish whether targeting cellular senescence with senolytics impacts facture healing dynamics. Herein, we specifically focus on fracture healing in young mice to avoid the confounding effects of senescence with aging. We first defined the transcriptional profiles of the healing callus and performed an in-depth characterization of cellular senescence at various timepoints. We then leveraged a *p16*^{Ink4a}-luciferase reporter mouse model (*p16*^{LUC}) *(19)* to further validate the appearance and disappearance of these cells *in vivo*. Finally, we treated young fractured mice with senolytics to evaluate whether clearance of senescent cells adversely affected fracture healing, which is a critical issue in the further development of senolytic therapies for osteoporosis.

bioRxiv preprint doi: https://doi.org/10.1101/2021.05.18.444618; this version posted May 19, 2021. The copyright holder for this preprint (which was not certified by peer review) is the author/funder, who has granted bioRxiv a license to display the preprint in perpetuity. It is made available under aCC-BY 4.0 International license.

Results

p21^{Cip1} and p16^{Ink4a} are induced during murine fracture healing

To evaluate transcriptome-wide changes underlying the different stages of fracture healing, we analyzed publicly available mRNA-seq data of murine femoral fracture sites as well as intact control femora at five specific time points *(20)*. At each time point, post-fracture femora displayed a distinct gene expression profile upon clustering (Figure 1A). Within this dataset, samples collected on day 7 and 14 diverged most from the freshly fractured and intact bone. To identify cellular processes affected by fracture- and healing-associated mRNA expression changes, we performed gene ontology analyses comparing intact controls to femora 14 days post-fracture. As expected, cellular processes related to cell proliferation as well as apoptosis were significantly enriched (Figure 1B, C). To detect key common regulators among those biological processes, components of the respective gene sets were overlapped. Interestingly, the cell cycle regulators *p21^{Cip1}* and *p16^{Ink4a}* were present in all gene lists (Figure 1D). Notably, the importance of p*16^{Ink4a}* and *p21^{Cip1}* during aging-associated bone deterioration has been previously observed by our group *(9,6)*. Next, gene expression kinetics of *p21^{Cip1}*, *p16^{Ink4a}*, as well as the proliferation marker *Mki67* were examined after the induction of femoral fracture. While the cell cycle-controlling genes displayed an increase from the baseline expression as compared to the contralateral intact femur, *Mki67* expression gradually decreased during bone healing (Figure 1E), indicating a decrease in proliferation. Together, these findings suggest a potential function of *p16^{Ink4a}* and *p21^{Cip1}* in regulating key cellular processes during fracture healing in mice with an emphasis on the late callus building phase around day 14.

bioRxiv preprint doi: https://doi.org/10.1101/2021.05.18.444618; this version posted May 19, 2021. The copyright holder for this preprint (which was not certified by peer review) is the author/funder, who has granted bioRxiv a license to display the preprint in perpetuity. It is made available under aCC-BY 4.0 International license.

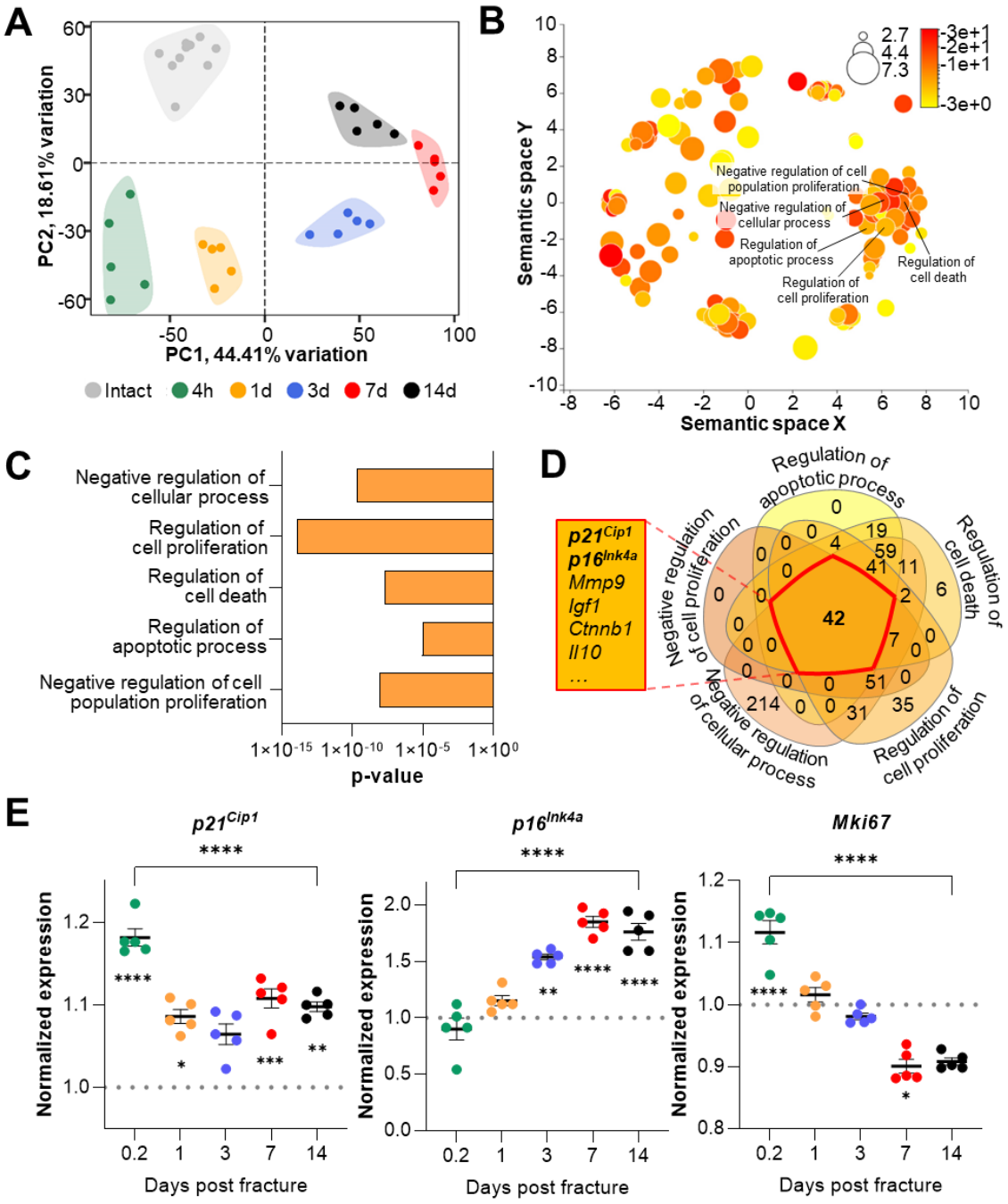

Figure 1: *p21*^{Cip1} and *p16*^{Ink4a} are upregulated after the induction of femoral fractures in mice. Transcriptome-wide changes during femoral fracture healing in mice were analyzed using publicly available mRNA-seq data (GSE152677 *(20)*). (A) Principal component analysis (PCA) illustrates the variance of gene expression profiles when comparing intact controls to fractured femora (0.2, 1, 3, 7 and 14 days post fracture; n=5 per time point). (B) Cellular pathways affected by gene expression changes 14 days after fracture compared to intact controls were detected using gene ontology (REVIGO;*(21)*). (C) REVIGO revealed that pathways associated with cell proliferation and cell death (GO:0048523, GO:0042127, GO:0010941, GO:0042981, GO: 0008285) were significantly affected 14 days after a mid-diaphyseal stabilized femoral fracture. (D) When overlapping these pathways, 42 genes were found to be present in all gene sets,

bioRxiv preprint doi: https://doi.org/10.1101/2021.05.18.444618; this version posted May 19, 2021. The copyright holder for this preprint (which was not certified by peer review) is the author/funder, who has granted bioRxiv a license to display the preprint in perpetuity. It is made available under aCC-BY 4.0 International license.

including *p21*^{Cip1} and *p16*^{Ink4a}. (E) Normalized mRNA expression kinetics reveal an upregulation of *p21*^{Cip1} and *p16*^{Ink4a} during fracture healing while *Mki67* levels decreased. The dotted line represents the normalized base line expression of intact control femora. The small asterisks indicate differences from the control. Mean ± SEM. One-way ANOVA; *p<0.05, **p<0.01, ***p<0.001, ****p<0.0001.

Senescent cells appear at fracture sites

For validation and extension of these *in silico* findings, we next induced femoral fractures in mice to further elucidate the possible roles of *p21*^{Cip1} and *p16*^{Ink4a} in fracture healing. After our *in silico* approach pointed to the end of the second week as the potential time point of highest senescent cell burden, we determined *p21*^{Cip1} and *p16*^{Ink4a} expression levels in the callus as well as the (intact) contralateral side after 4, 8, 14 and 28 days (Figure 2A). Notably, we detected a 20-fold increase in *p21*^{Cip1} and a 100-fold increase in *p16*^{Ink4a} 14 days post fracture compared to the contralateral side (Figure 2B). Due to the major function of *p21*^{Cip1} and *p16*^{Ink4a} in regulating cellular senescence *(9,10)*, we next tested for the presence of the most specific markers for cellular senescence by assessing senescence-associated distension of satellites (SADS) and telomere-associated DNA-damage foci (TAF) within the callus *(22,2)*. For this purpose, we performed immuno-fluorescent *in situ* hybridization (FISH) in the callus area after fracturing and stabilizing femora with an intramedullary pin. This analysis demonstrated that the number of SADS-positive senescent cells *(9)* in the callus was higher by ~6-fold with a peak on days 8 and 14 relative to the contralateral control (Figure 2C, D). In agreement with this finding, the fractured side contained more TAF-positive senescent cells (Figure 2E, F). Indeed, the number of TAF-positive senescent cells was highest in the fracture callus on day 14 and higher than in the contralateral side throughout the entire observational period (Figure 2F), mirroring the changes in senescence genes and SADS over the time course. In summary, the murine callus displays a profound induction of *p21*^{Cip1} and *p16*^{Ink4a} expression as well as specific cellular senescence markers (SADS and TAF) 14 days after a femoral fracture.

bioRxiv preprint doi: https://doi.org/10.1101/2021.05.18.444618; this version posted May 19, 2021. The copyright holder for this preprint (which was not certified by peer review) is the author/funder, who has granted bioRxiv a license to display the preprint in perpetuity. It is made available under aCC-BY 4.0 International license.

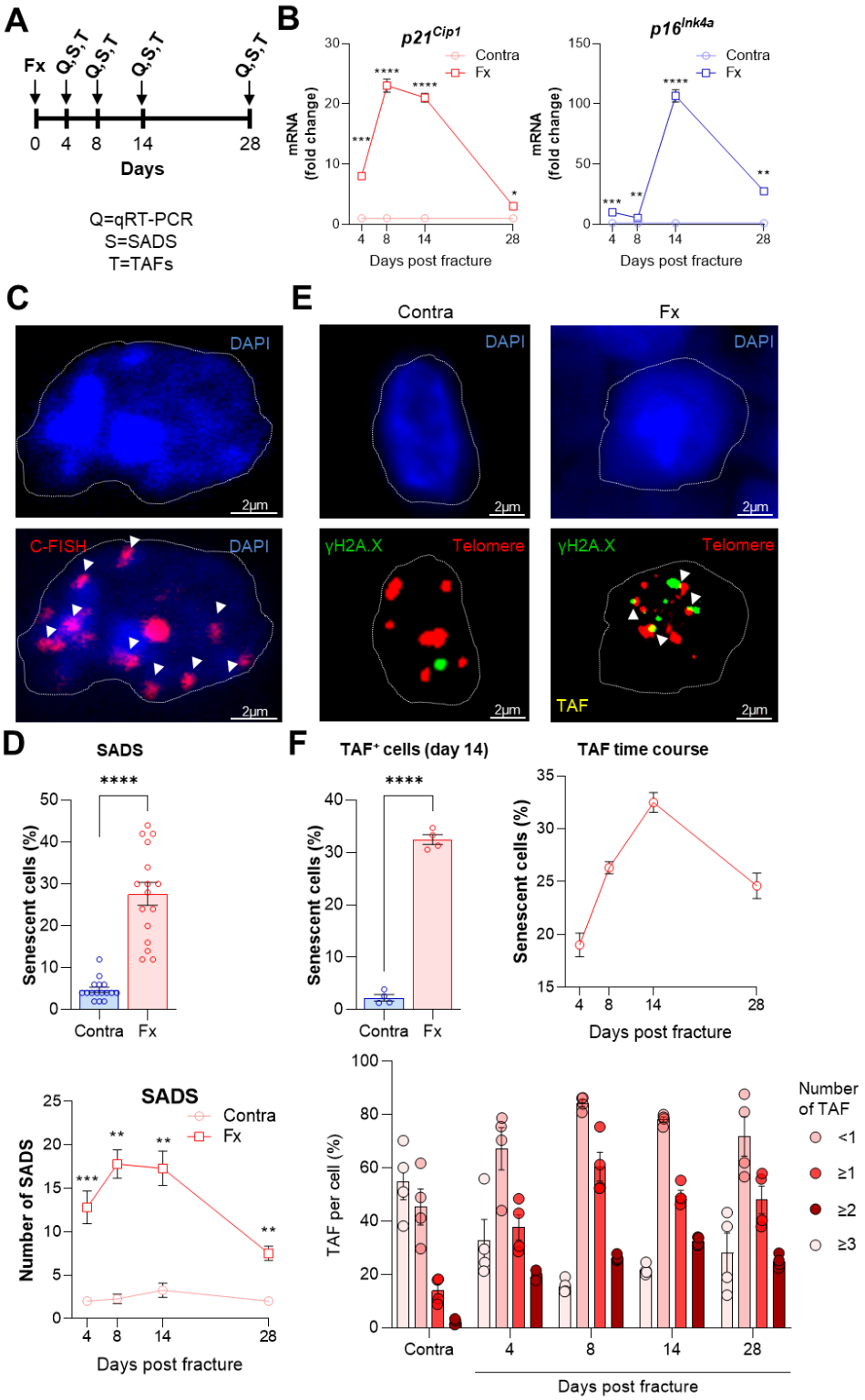

Figure 2: Cellular senescence is induced during femoral fracture healing. (A) Femoral fractures (Fx) were induced in male C57BL/6 mice with contralateral (Contra), intact control femora. Callus and controls were analyzed 4, 8, 14 and 28 days after fracture (n=4 per time point). (B) *p21*^{Cip1} and *p16*^{Ink4a} mRNA expression levels during fracture healing were determined at each

bioRxiv preprint doi: https://doi.org/10.1101/2021.05.18.444618; this version posted May 19, 2021. The copyright holder for this preprint (which was not certified by peer review) is the author/funder, who has granted bioRxiv a license to display the preprint in perpetuity. It is made available under aCC-BY 4.0 International license.

time point using qRT-PCR. *p21^{Cip1}* was strongly induced 8-14 days and *p16^{Ink4a}* 14 days post fracture. (C) Senescence-associated distension of satellites (SADS) were detected using immune-fluorescent *in situ* hybridization (FISH) Top: representative image of the contralateral side. Below: fractured side with four SADS. (D) The total number of SADS as well as percentage of SADS-positive cells (≥4 SADS/cell) at all time points was increased in the callus compared to the contralateral control femur. (E) Telomere-associated foci (TAF) were determined using FISH to detect telomeres (red) and immunofluorescent staining for γH2A.X (green). TAF (yellow, see arrowheads) were defined as sites of γH2A.X-associated DNA damage co-localized with telomeres (n=70 cells were analyzed per bone). (F) The highest percentage of TAF were detected on day 14 of fracture healing. The number of TAF-positive senescent cells (≥3 TAF/cell) was increased in fractured bones throughout the entire healing period. Mean ± SEM. One-way ANOVA or Student's *t*-test for pairwise comparisons; *p<0.05, **p<0.01, ***p<0.001, ****p<0.0001.

p16^{Ink4a}-expressing cells accumulate in the callus in vivo and homozygous deletion of p16^{Ink4a} increases callus volume

After observing the induction of senescence and upregulation of *p16^{Ink4a}* in the fracture callus, we sought to confirm the accumulation of *p16^{Ink4a}* -expressing cells *in vivo* at the fracture site and evaluate the effects of homozygous deletion of *p16^{Ink4a}* on fracture healing. For this purpose, we utilized *p16^{LUC}* mice, in which the firefly luciferase cDNA is knocked in into the translational start site of the endogenous *p16^{INK4a}* locus *(19)*. Thus, these mice serve as both reporter mice for *p16^{Ink4a}* expression and, in the homozygous state, are a complete *p16^{Ink4a}* knock out. Upon fracture induction, *p16^{Ink4a}* -positive cells were visualized using bioluminescence (Figure 3A, B). *p16^{Ink4a}*-driven luminescence peaked approximately two weeks after fracture induction and was nearly undetectable after day 18 (Figure 3C). Notably, *p16^{Ink4a}* luminescence kinetics mirrored the time course of *p16^{Ink4a}* mRNA expression we observed *in silico* and *ex vivo* and also paralleled the changes in SADS and TAF we observed as described above (Figure 1E, 2C-E). We also analyzed the consequences of *p16^{Ink4a}*-knockout on the time course of bone healing by weekly X-ray analyses performed according to Wehrle et al. *(23)* (Figure 3D) and measurements of the relative callus area (Figure 3E, F). Although the overall time course of healing was not significantly altered in the *p16^{Ink4a}*-deficient mice, post-mortem end point analysis revealed that the callus bone volume was significantly increased in these mice relative to the wild type mice (Figure 3G). These findings thus demonstrate that *p16^{Ink4a}*-positive cells accumulate at the fracture site *in vivo* and that complete loss of *p16^{Ink4a}* expression does not impair, but rather increases callus volume during fracture healing.

bioRxiv preprint doi: https://doi.org/10.1101/2021.05.18.444618; this version posted May 19, 2021. The copyright holder for this preprint (which was not certified by peer review) is the author/funder, who has granted bioRxiv a license to display the preprint in perpetuity. It is made available under aCC-BY 4.0 International license.

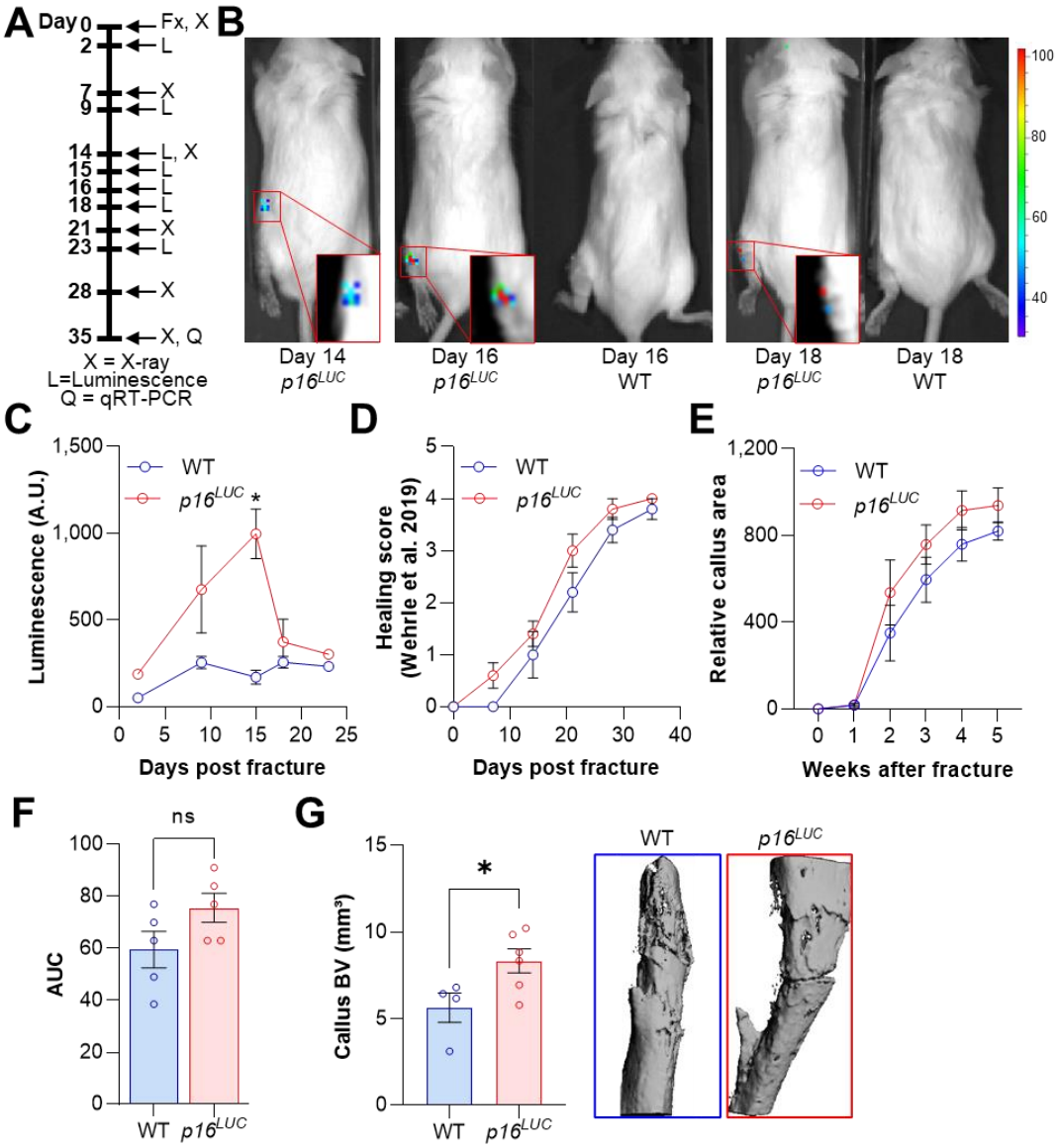

Figure 3: *p16*^{Ink4a}-positive cells are present at the fracture site and negatively affect callus formation. The involvement of *p16*^{Ink4a}-expressing cells in callus was evaluated in *p16*^{LUC} or wild type (WT) mice (n=10 per genotype). (A) Tibial fractures (Fx) were induced and *p16*^{Ink4a}-dependent luminescence was analyzed between 2 and 23 days after fracture using Xenogen. X-rays were performed weekly and callus was isolated at day 28 for subsequent qRT-PCR. (B) Representative Xenogen images of *p16*^{Ink4a}-associated luminescence at fracture sites in *p16*^{LUC} mice. (C) Luminescence corresponding to *p16*^{Ink4a}-expression after tibial fracture in WT and *p16*^{LUC} mice as detected using Xenogen. *p16*^{Ink4a}-associated luminescence reached its maximum 15 days after fracture while no signal was detected in WT controls. (D) Bone healing was scored based on X-ray analysis according to Wehrle and colleagues *(23)*. Healing kinetics were similar among genotypes. (E) Relative callus area was quantified after X-ray analysis using FIJI. (F) *p16*^{LUC} mice displayed a trend towards an increase in callus area as determined by calculating the area under the curve (AUC, p=0.11). (G) Callus bone volume (BV) was measured and visualized postmortem using micro-CT. The depletion of *p16*^{Ink4a}-expressing cells resulted in

bioRxiv preprint doi: https://doi.org/10.1101/2021.05.18.444618; this version posted May 19, 2021. The copyright holder for this preprint (which was not certified by peer review) is the author/funder, who has granted bioRxiv a license to display the preprint in perpetuity. It is made available under aCC-BY 4.0 International license.

significantly elevated callus BV. Mean ± SEM. One-way ANOVA or Student's *t*-test for pairwise comparisons; *p<0.05, **p<0.01, ***p<0.001, ****p<0.0001.

Senescent cells and the SASP show distinct expression patterns in the fracture callus.

Along with the appearance of cellular senescence, a locally detrimental bystander effect is caused by the $p21^{Cip1}$- and $p16^{Ink4a}$-positive cells via SASP secretion *(24,25)*. As such, we performed a detailed analysis using qRT-PCR of the fracture callus over time. The SASP consists of, among others, growth factors and growth regulators (Figure 4A), out of which *Igfbp3* showed a 20-fold increase by day 14. Remarkably, the chemokine *Ccl7* was more than 70-fold increased on day 14 (Figure 4B). The protease Plasminogen activator inhibitor-1 (*Pai1* or *Serpine1*) was elevated by more than 60-fold on day 8 but declined substantially on day 14 (Figure 4C). Several transcription factors, including *Nfkb1*, showed a modest increase, while *Foxo4* was significantly increased on day 8 and 14 (Figure 4D). In the TGFβ complex, *Tgfb1* itself displayed an initial increase and then a substantial decrease on day 28 which was even significantly lower than levels detected in the intact bone (Figure 4E). Several members of the interleukin family such as *Il6* and *Il17a* showed the typical rise within the first days of the fracture (inflammatory phase) whereas *Il1b* was downregulated (Figure 4F). Overall, the expression pattern of all senescence-associated and SASP genes was highly heterogeneous (Supplementary Figure S1). However, distinct gene clusters displaying similar patterns could be constructed. For example, $p16^{Ink4a}$ and $p21^{Cip1}$ were detected within a cluster consisting of growth factors (*Igfbp3*, *Igfbp4*, *Vegfa*), proteases (*Mmp13*), and transcription factors (*Foxo4*). The similarity in regulation was indicated by their high correlation coefficients (Figure 4G). To determine which cell population may be associated with SASP secretion, we analyzed a publicly available single cell dataset (*(26)*, Supplementary Figure S2A). After evaluating key regulators within murine bone and marrow, we found the highest enrichment of SASP genes within the mesenchymal stem cell (MSC) cluster (Supplementary Figure S2), which helped guide the subsequent studies below.

bioRxiv preprint doi: https://doi.org/10.1101/2021.05.18.444618; this version posted May 19, 2021. The copyright holder for this preprint (which was not certified by peer review) is the author/funder, who has granted bioRxiv a license to display the preprint in perpetuity. It is made available under aCC-BY 4.0 International license.

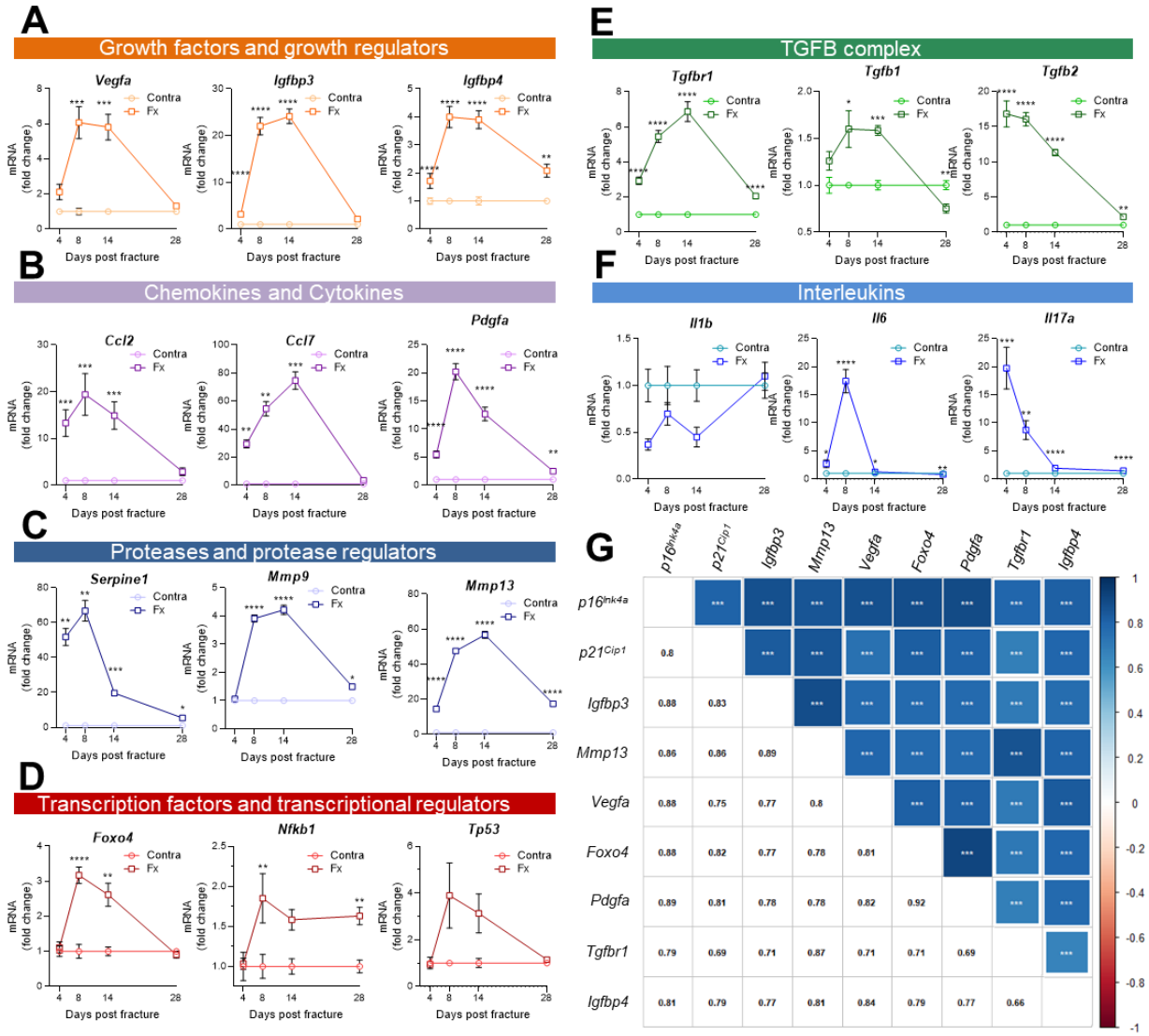

Figure 4: Multiple SASP factors show a marked increase in the healing callus, while distinct genes form similarly behaving clusters. SASP-associated factors can be subdivided into functional subunits. (A) mRNA expression of the growth factors *Vegfa*, *Igfbp3* and *Igfbp4* substantially increased during the callus forming phase (day 2-15). (B) The chemokines *Ccl2* and *Pdgfa* more profoundly rose in gene expression levels in the soft callus (day 2-7) but not in the hard callus (day 8-14) phase, while *Ccl7* was more than 70-fold increased on day 14. (C) Expression of the protease *Serpine1* was elevated in the soft callus phase, similar to *Pdgfa*, while *Mmp9* and *Mmp13* peaked on day 14. (D) The transcription factors *Foxo4*, *Nfkb1* and *Tp53* peaked on day 8, marking the beginning of hard callus formation. (E) TGFβ-associated genes displayed heterogeneous expression patterns. While *Tgfbr1* peaked on day 14, *Tgfb1* reached a plateau on day 8 and 14, and *Tgfb2* gradually declined after an initial peak on day 4. (F) Among the interleukins, *Il1b* was negatively regulated in the beginning of the healing phase, while *Il6* shortly peaked in the inflammatory and soft callus phase. *Il17a* showed a gradually decline, comparable to *Tgfb2*. (G) The largest cluster displaying similar gene expression patterns among all senescence-associated and SASP-gene markers included the key cell cycle regulators *p16*^{Ink4a} and *p21*^{Cip1}. The square size is proportional to the correlation coefficient, which is also depicted

bioRxiv preprint doi: https://doi.org/10.1101/2021.05.18.444618; this version posted May 19, 2021. The copyright holder for this preprint (which was not certified by peer review) is the author/funder, who has granted bioRxiv a license to display the preprint in perpetuity. It is made available under aCC-BY 4.0 International license.

in the left bottom corner. Significant results were indicated with asterisks. Mean ± SEM. Multiple *t*-test (FDR); *p<0.05, **p<0.01, ***p<0.001, ****p<0.0001.

Senescence in MSCs can be partially rescued by senolytic treatment in vitro

Based on the above experimental and *in silico* analyses, we next aimed to determine the effects of senolytics on MSCs *in vitro*. For this purpose, MSCs were isolated from murine bone marrow, cultured *in vitro* until confluent, and then treated with D+Q. The senolytic cocktail did not exert effects on cell numbers (Figure 5A, B). Subsequently, the cells were treated with 100 µM H_2O_2 to induce senescence (Figure 5C, D). Senescent cells were detected using SA-β-Gal staining and, as anticipated, addition of H_2O_2 resulted in profound cellular senescence (Figure 5D). Treatment with D+Q rescued this effect by significantly reducing the percentage of senescent cells from 33.1% to 13.1% (-60.3%; Figure 5C, D). Next, we treated mice with vehicle or D+Q *in vivo* and extracted MSCs to grow them *ex vivo* (Figure 5E). The relative cell number of isolated MSCs was increased after five weeks of D+Q treatment *in vivo* (Figure 5F) while SA-β-Gal staining revealed a minor reduction in the number on senescent cells (-18.8%, Figure 5 G, H). However, a priori *in vivo* treatment with D+Q did not significantly reduce the proportion of cells becoming senescent after H_2O_2 treatment (Figure 5 G, H). Together, our *in vitro* studies suggest that H_2O_2-induced senescence in MSCs can be partially rescued by D+Q treatment.

bioRxiv preprint doi: https://doi.org/10.1101/2021.05.18.444618; this version posted May 19, 2021. The copyright holder for this preprint (which was not certified by peer review) is the author/funder, who has granted bioRxiv a license to display the preprint in perpetuity. It is made available under aCC-BY 4.0 International license.

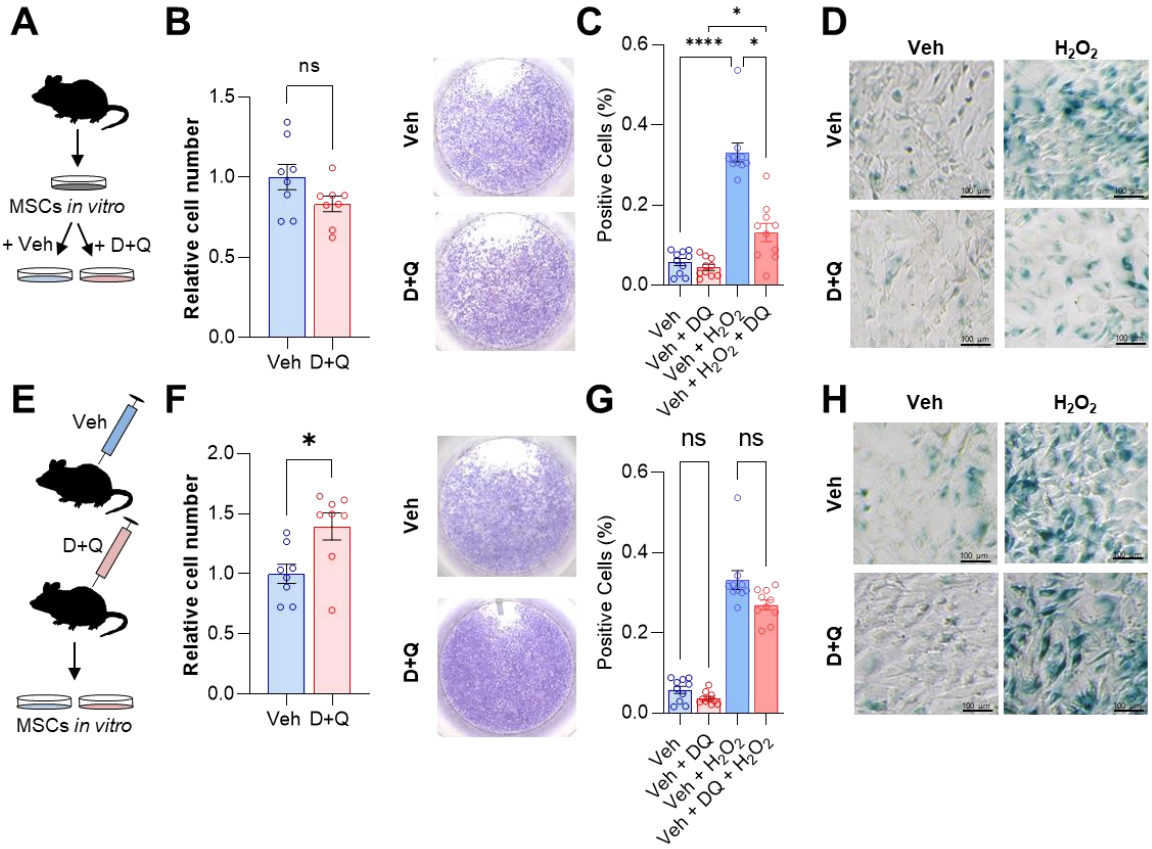

Figure 5: D+Q treatment can partially rescue senescence in MSCs *in vitro*. (A) Bone marrow MSCs were isolated from wild type mice and grown *in vitro* until a confluence of approximately 70% was observed. (B) After seeding the same cell numbers, MSCs were incubated with 200 nM Dasatinib and 50 µM Quercetin (D+Q) or vehicle solution for 24 hours. Relative cell numbers were evaluated 24 h after D+Q or vehicle treatment (n=6 per treatment). Besides using an automated cell counter, cells were stained using crystal violet to visualize cell densities. D+Q treatment did not change relative cell numbers. (C) MSCs were treated with 100 µM H_2O_2 for 4 h to induce senescence, washed with PBS and cultured for another three days. Afterwards, cells were treated with D+Q or vehicle solution for 24 h. After fixation, senescent cells were visualized using SA-β-Gal staining and quantified using FIJI (n=4). (D) Representative images of SA-β-Gal staining. While H_2O_2 induced senescence, this effect was rescued by subsequent D+Q treatment. (E) Wild type mice were treated with 5 mg/kg BW Dasatinib and 50 mg/kg body weight Quercetin or vehicle solution via oral gavage weekly for 5 weeks. Bone marrow MSCs were isolated and cultured *in vitro*. (F) Relative cell number of D+Q-treated mice was increased 48 h after seeding the same cell numbers (n=6). Cell confluence was visualized using crystal violet staining. (G) *In vivo* treatment with D+Q resulted in a minor reduction in the number on senescent cells. H_2O_2 treatment induced cellular senescence in a comparable manner to the previous approach (Figure 5C). (H) Representative images of SA-β-Gal staining. An *a priori in vivo* treatment with D+Q did not significantly reduce the proportion of cells becoming senescent after H_2O_2 treatment. Mean ± SEM. One-way ANOVA or Student's *t*-test for pairwise comparisons; *p<0.05, **p<0.01, ***p<0.001, ****p<0.0001.

Pharmacological clearance of senescent cells does not impair but rather accelerates the time course of fracture healing in vivo

bioRxiv preprint doi: https://doi.org/10.1101/2021.05.18.444618; this version posted May 19, 2021. The copyright holder for this preprint (which was not certified by peer review) is the author/funder, who has granted bioRxiv a license to display the preprint in perpetuity. It is made available under aCC-BY 4.0 International license.

Based on our findings with the *p16*^{Ink4a} knock out mice and D+Q effects on senescent MSCs *in vitro*, we hypothesized that, in contrast to skin wound healing *(15)*, clearance of senescent cells using D+Q treatment would enhance fracture healing *in vivo*. To test this, we treated wild-type mice with D+Q one day before fracture and on a weekly basis post fracture (Figure 6A). Based on our previous experiments where markers of senescence peaked on day 14 (Figure 1E, 2B-F), we sacrificed one mouse cohort at this time point and performed gene expression analysis of callus tissue. The senescence and SASP markers *p16*^{Ink4a}, *Pdgfa* and *Foxo4* displayed decreased mRNA levels in response to D+Q treatment (Figure 6B) along with additional SASP factors (Supplementary. Figure S3A); of interest, some factors (e.g., *Gdf15* and *Pdgfb*) increased following D+Q treatment (Supplementary Figure S3A). The reduction of *p16*^{Ink4A} mRNA was confirmed at the protein level (Figure 6C). To address the impact of D+Q treatment on fracture healing, weekly X-rays were performed and tibia healing was classified according to Wehrle et al. *(23)*. Notably, we detected significantly improved healing kinetics after the clearance of senescent cells with D+Q treatment (Figure 6D). Weekly two-plane assessments of the callus area confirmed an increased callus area two weeks after fracture (Figure 6E, F). In addition, the relative callus area was already reduced by week 5 in the D+Q group, indicating an accelerated callus restoration (i.e. earlier approach to the remodeling phase) after the maximum area had been reached (Figure 6F). Micro-CT analysis after 5 weeks demonstrated a trend toward higher callus volume in D+Q-treated mice (Figure 6G). Finally, we evaluated biomechanical properties of healed tibiae. In agreement with the elevated callus area and higher healing score on day 14, yet convergence at the end of the healing phase, senolytic treatment resulted only in a trend for increased bone stiffness (Figure 6H). Thus, D+Q treatment reduced gene expression levels of senescence markers/SASP markers and, in contrast to findings in skin wound healing *(15)*, did not impair but rather accelerated the time course of fracture healing.

bioRxiv preprint doi: https://doi.org/10.1101/2021.05.18.444618; this version posted May 19, 2021. The copyright holder for this preprint (which was not certified by peer review) is the author/funder, who has granted bioRxiv a license to display the preprint in perpetuity. It is made available under aCC-BY 4.0 International license.

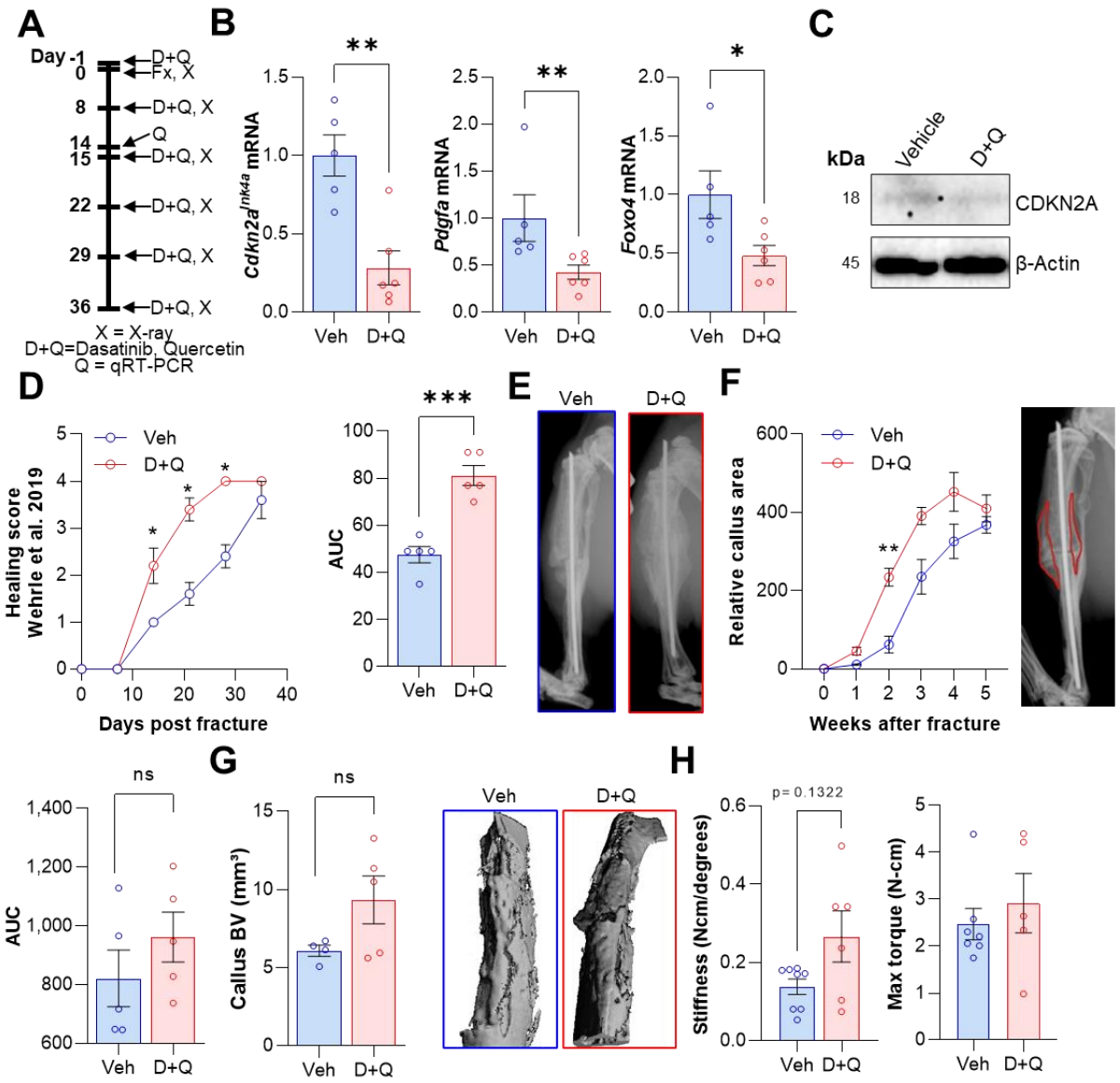

Figure 6: D+Q treatment accelerates the time course of fracture healing. Senescent cells were cleared by oral gavage of wild type mice one day before tibial fracture and weekly with 5 mg/kg BW Dasatinib and 50 mg/kg BW Quercetin or vehicle solution (n=10 per group). Half of the respective cohorts were sacrificed after 14 days for gene expression analyses while the remaining animals were treated with D+Q weekly for a total of 5 weeks. (A) mRNA levels of the SASP markers *p16*^{Ink4a}, *Pdgfa* and *Foxo4* were reduced by D+Q treatment 14 days after fracture induction as detected using qRT-PCR. (C) Western blot analysis of callus material revealed reduction of p16^{INK4A} protein level in the D+Q cohort. (D) Bone healing was assessed using X-ray analysis according to Wehrle et al. *(23)*. Bone healing was significantly elevated by D+Q administration. (E) Representative X-ray images of vehicle- and D+Q-treated mice 14 days after tibial fracture. Callus volume appeared to be increased in the D+Q cohort. (F) Relative callus area was detected after X-ray analysis and quantification using FIJI, showing an acceleration in the time course of callus formation. (G) Callus bone volume at 5 weeks determined using micro-CT trended to be increased in D+Q-treated mice. (H) Biomechanical analysis of the tibiae revealed a non-significant increase of bone stiffness and maximum torque upon senolytic treatment. Mean ±

bioRxiv preprint doi: https://doi.org/10.1101/2021.05.18.444618; this version posted May 19, 2021. The copyright holder for this preprint (which was not certified by peer review) is the author/funder, who has granted bioRxiv a license to display the preprint in perpetuity. It is made available under aCC-BY 4.0 International license.

SEM. One-way ANOVA or Student's *t*-test for pairwise comparisons; *p<0.05, **p<0.01, ***p<0.001, ****p<0.0001.

bioRxiv preprint doi: https://doi.org/10.1101/2021.05.18.444618; this version posted May 19, 2021. The copyright holder for this preprint (which was not certified by peer review) is the author/funder, who has granted bioRxiv a license to display the preprint in perpetuity. It is made available under aCC-BY 4.0 International license.

Discussion

Cellular senescence is generally considered in the context of its adverse effects during aging *(27)*. Clearance of senescent cells has been shown to reverse age-associated symptoms and diseases in mice and senolytic therapies are now in early phase clinical trials for a range of age-associated disorders *(28,29,1)*. Similarly, clearance of *p16^{Ink4a}*-positive senescent cells using genetic approaches has been shown to reduce age-associated diseases and increase healthspan in mice *(3,30,5,31,8)*. However, previous studies in skin wound healing have suggested a beneficial role of transiently appearing senescent cells in that process *(15)*. This, in large part, has formed the basis for the hypothesis that senescent cells, although detrimental in the context of aging, may be beneficial for tissue repair via the secretion of the SASP, in part by attracting immune cells and initiating the tissue repair process *(32)*. However, whether this concept holds true across tissues beyond the skin is of considerable importance, particularly for the potential translation of senolytic therapies for osteoporosis. Indeed, a detrimental effect of senescent cell clearance on fracture repair would pose perhaps a fatal roadblock for the development of senolytic therapies for osteoporosis. Relevant to this issue, we demonstrate senescent cells in the dynamically healing bone and define the time course of appearance and subsequent disappearance of these cells from the fracture callus. Importantly, using both a genetic and pharmacological model, we reduce the senescent cell burden and demonstrate no adverse effects, but rather beneficial effects (i.e., increased callus volume in the *p16^{Ink4a}* knock out model and accelerated time course of healing with senolytics) on fracture healing.

As noted earlier, we focused this initial study on young mice in order to avoid potential confounding due to aging and to define the possible physiological role of senescent cells in fracture healing. At a gene expression level and using two independent post-transcriptional techniques (SADS and TAF), which are the most specific markers for cellular senescence *(9,33,34)*, we were able to first describe the appearance of senescent cells within the physiologically healing murine bone. Moreover, we established a time-course of cellular senescence peaking on day 14 in healing long bones and made use of a genetic knockout model of *p16^{Ink4a}*, the *p16^{LUC}* mouse, to both visually detect and assess the role of *p16^{Ink4a}* knock out on fracture healing. In line with the findings by Demaria et al. in skin wound healing *(15)*, a transient increase of *p16^{Ink4a}*-positive cells was detected in the final stages of the anabolic and beginning catabolic phase of fracture healing. The healing process itself, however, was not fundamentally changed by the functional reduction of *p16^{Ink4a}* but the callus volume was significantly enhanced in mice with *p16^{Ink4a}* deletion relative to wild type controls.

bioRxiv preprint doi: https://doi.org/10.1101/2021.05.18.444618; this version posted May 19, 2021. The copyright holder for this preprint (which was not certified by peer review) is the author/funder, who has granted bioRxiv a license to display the preprint in perpetuity. It is made available under aCC-BY 4.0 International license.

The role of the SASP in the skeletal system has mostly been shown to be adverse *(35,36,4)*. We demonstrate here a substantial increase in the SASP during fracture healing, with some SASP factors increasing during the inflammatory phase and others in early and late callus forming phases. Although multiple approaches have been used to subclassify the SASP *(37–40)*, we for the first time elucidated its components within healing bone and found specific $p16^{Ink4a}$ and $p21^{Cip1}$ clusters of associated SASP factors with a concordant time course during fracture healing. Elucidating the potential therapeutic applicability of these findings, we made use of a first-generation senolytic cocktail, D + Q. This treatment has successfully moved from preclinical studies after reducing the cellular senescence burden in bone *(6)* and adipose tissue *(8)* and is currently in multiple clinical trials, including for the prevention and/or treatment of osteoporosis (NCT04313634). We demonstrated its efficiency in reducing MSC senescence *in vitro* and treated healing murine long bones *in vivo* with this senolytic regimen. Following senolytic treatment, the senescence marker $p16^{Ink4a}$ was substantially reduced, along with a number of SASP markers. The time course of bone healing was accelerated, and biomechanical bone parameters modestly enhanced. Notably, some SASP markers, specifically *Gdf15* and *Pdgfb*, were increased after the senolytic treatment. It has been hypothesized that up to a certain threshold, a transient senescent burden may be favoring healing (e.g., skin wounds), while above this threshold there may be a failure of wound closure, as observed in chronic wounds *(41–43)*. Our findings suggest that cellular senescence in healing bone follows a transient time course that peaks around the second week of fracture healing, thereby potentially suppressing callus formation. Given that senolytics do not kill all senescent cells, but rather reduce their proportion (*e.g.,* by ~30% *(44)*), our data demonstrate that this reduction is sufficient to enhance callus formation and at least does not impair the biomechanical properties of the healed bone.

In addition to implications for senolytic therapies for osteoporosis, our findings also have potential biological implications. Specifically, the concept of senescent cells as physiologically facilitating tissue repair which, to date, has been definitively demonstrated principally in the skin *(15)* may be overly simplistic. Thus, contrary to the skin and uniquely in the living organism, bone has the ability to fully recover without losing its integrity and form a scar. As such, it is possible that the transient appearance of senescent cells is an evolutionarily conserved mechanism during injury repair, with beneficial effects on skin wound healing, which is associated with scar formation. By contrast, the lack of scar formation in bone and the already highly inflammatory state following fracture *(16)* may render these transiently appearing senescent cells less useful and, as demonstrated in our study, potentially detrimental, to injury repair in bone. Clearly, further studies

bioRxiv preprint doi: https://doi.org/10.1101/2021.05.18.444618; this version posted May 19, 2021. The copyright holder for this preprint (which was not certified by peer review) is the author/funder, who has granted bioRxiv a license to display the preprint in perpetuity. It is made available under aCC-BY 4.0 International license.

are needed to test this hypothesis, but our findings should stimulate a reconsideration of senescent cells as generally beneficial in the setting of tissue injury and repair.

In summary, we demonstrate that cellular senescence is present in fracture callus development using both transcriptional and more specific analyses evaluating telomeric DNA damage, a hallmark of cellular senescence *(2)*. We established the time course of *p16^{Ink4a}* or *p21^{Cip1}* expression during fracture healing, associated well-described SASP components to these key senescent genes, and reduced the senescent burden with senolytic drugs. Importantly, this approach did not impair, but rather enhanced the fracture healing process *in vivo*. Collectively, our findings have clinical implications for the development of senolytic therapies for osteoporosis and also have biological relevance for our concept of senescent cells as facilitating healing, as these beneficial versus detrimental effects of senescent cells on injury repair may vary across tissues.

bioRxiv preprint doi: https://doi.org/10.1101/2021.05.18.444618; this version posted May 19, 2021. The copyright holder for this preprint (which was not certified by peer review) is the author/funder, who has granted bioRxiv a license to display the preprint in perpetuity. It is made available under aCC-BY 4.0 International license.

Materials and methods

Animal studies. Animal studies were performed under protocols approved by the Institutional Animal Care and Use Committee (IACUC), and experiments were performed in accordance with Mayo Clinic IACUC guidelines. All assessments were performed in a blinded fashion. Mice were housed in ventilated cages and maintained within a pathogen-free, accredited facility under a twelve-hour light/dark cycle with constant temperature (23°C) and access to food (diet details are specified below) and water ad libitum. We used young adult male and female C57BL/6N mice (starting at four months, ending at five to six months of age) for our experimental procedures. For anesthesia during surgery, we used isoflurane (vaporizer, 1.5-2% in oxygen, inhalation) for induction and maintenance until the surgery was complete (about 20 min).

A schematic of the study design in each of the three study phases (WT, $p16^{LUC}$, D+Q) and respective timelines for the treatments is shown in Figure 2A, 3A, and 6A.

For the first study (WT), four-month-old male C57BL/6N WT mice (n=16) of comparable mean body weights received a standardized, closed diaphyseal femoral fracture. After a lateral parapatellar knee incision, the left femur was exposed while the tendons and muscles were protected. After that, a transverse osteotomy with a rotary bone saw was introduced. An Insect Pin (Fine Science Tools, 26001-30, Austerlitz Insect Pin rod diameter 0.03 mm) was inserted retrogradely from the trochlear groove to stabilize the transverse femoral shaft fracture. After wound closure, postoperative pain management was performed with subcutaneous buprenorphine hydrochloride (0.1 mg/kg body weight [BW]) and the correct position of the pin was immediately affirmed by X-ray. Normal weight bearing postoperatively was allowed. X-rays were performed on a weekly basis as described in Radiographical fracture healing assessment. For each timepoint (4, 8, 14, 28 days), n=4 male mice per time point were used (n=16 mice in total).

For the $p16^{LUC}$ study, Alb.B6.p16-Luciferase mice were used as described in detail elsewhere *(19)*. $p16^{LUC}$ mice were used: Alb.B6.p16-Luciferase mice (n=8 $p16^{WT/WT}$ and n=8 $p16^{LUCLUC}$, herein referred to as WT and $p16^{LUC}$, respectively) with a homogenous Alb.B6.$p16^{Luc/Luc}$ and their littermates were used. Here, we performed a left transverse tibia fracture. The mid-shaft tibia was incised along the anterior side of the tibia, and an unilateral transverse osteotomy with a rotary bone saw was performed. The fractured bone was stabilized with an intramedullary Insect Pin was retrogradely implemented *(45)*. X-rays and pain management was performed as described

bioRxiv preprint doi: https://doi.org/10.1101/2021.05.18.444618; this version posted May 19, 2021. The copyright holder for this preprint (which was not certified by peer review) is the author/funder, who has granted bioRxiv a license to display the preprint in perpetuity. It is made available under aCC-BY 4.0 International license.

in the WT study. In addition to weekly X-rays, luminescence was detected (see Bioluminescence). The bioluminescence assay was performed in n=8 mice, while two additional mice received weekly X-rays.

For the D+Q study, 4-month-old C57BL/6 mice (n=20) were randomized to either vehicle (Veh) or Dasatinib plus Quercetin (D+Q) treatment on a weekly basis (Figure 6A). Vehicle or D+Q was administered via oral gavage. The weekly treatment regimen was verified to be effective in eliminating senescent cells by our group previously *(6)*. Senolytics were diluted in 10% EtOH, 30% PEG, 60% Phosal-50and administered via oral gavage at dosages of 5 mg/kg BW Dasatinib and 50 mg/kg BW Quercetin, respectively, in a total volume of 100 µl. The surgical procedure was performed as described above and weekly X-rays were carried out to indicate the fracture healing course. Post mortem, both intact and fractured tibiae were stored in 0.9% saline (NaCl)-soaked gauze at -20°C for direct scanning with *ex vivo* micro-computed tomography (micro-CT) (see Skeletal imaging) and subsequent biomechanical strength testing by standardized rotational testing (see torsional testing).

Mouse tissue collection and assessments. Prior to sacrifice, body mass (g) was recorded and serum was collected in the morning under fasting conditions from anesthetized mice via cardiac puncture and stored at -80°C. In the $p16^{LUC}$ and D+Q study, tibiae, femora and humeri were excised from the mice and skeletal muscle/connective tissues were removed after euthanasia. The left tibia was stored in 0.9% saline (NaCl) soaked gauze at -20°C for direct *ex vivo* micro-computed tomography (micro-CT) scanning (see Skeletal imaging) and subsequent biomechanical strength testing by standardized torsional testing (see torsional testing). In the WT study, both non-decalcified femora were embedded in methyl-methacrylate and sectioned for immunohistochemistry (IHC) (see Skeletal histomorphometry assessments), and fluorescent in situ hybridization (FISH) (see Senescence-associated distension of satellites [SADS]).

In the D+Q study, the right tibia, both femora and both humeri were used to extract and culture bone marrow stem cells (BMSC; see Cell culture experiments). In the D+Q study and WT study, for fracture RNA analysis, the pin was removed, and the visually verified callus area removed after cleaning the bone from surrounding tissue. This callus area was minced with a scalpel in FACS buffer, and homogenized in QIAzol Lysis Reagent (QIAGEN, Valencia, CA), and frozen at -80°C for real-time quantitative polymerase chain reaction (qRT-PCR) mRNA gene expression analyses (see Real-time quantitative polymerase chain reaction analysis).

bioRxiv preprint doi: https://doi.org/10.1101/2021.05.18.444618; this version posted May 19, 2021. The copyright holder for this preprint (which was not certified by peer review) is the author/funder, who has granted bioRxiv a license to display the preprint in perpetuity. It is made available under aCC-BY 4.0 International license.

Skeletal imaging: Radiographical fracture healing assessment. All imaging and analysis was performed in a blinded fashion as described by our group previously *(17)*. Briefly, radiographs of the fractured femora or tibiae were taken under anesthesia after surgery and on a weekly basis. Therein, mice were in a supine position and both limbs extended. Anteroposterior (ap) and lateral (lat) planes were assessed. Radiographs were evaluated by two blinded researchers and scored for fracture healing using the score by Wehrle et al. *(23)* and Undale et al. *(17)*. After a satisfactory accordance was obtained (R^2=0.89, Supplementary Figure. S3B), we decided to report the initially CT-based score by Wehrle et al. only, since the two planes gave us a good representation of all four cortices. The radiographs of fracture callus were quantified and analyzed with FIJI (NIH, Bethesda, MD, USA), as described elsewhere *(46)*.

Skeletal imaging: Ex vivo micro-CT imaging. At study endpoint, callus volume of the left (fractured) tibia (proximal metaphysis to distal metaphysis) was performed. Scan settings were: 55 kVp, 10.5 µm voxel size, 21.5 diameter, 145mA, 300 ms integration time. For the callus volume measurement, a threshold of 190 and 450 were chosen according to the manufacturer's protocols (Scanco Medical AG, Basserdorf, Switzerland).

Bioluminescence. In vivo luminescence was measured with a Xenogen IVIS Spectrum instrument and Living Image software (5 min medium binning). Bioluminescent signal quantification (photons/s/cm^2/sr) of the fracture region was measured with the Living Image software. Mice were i.p. injected with 15 µg of Xenolight RediJect Coelentarazine h (Calipers). After 25 minutes, mice were anesthetized with isoflurane and imaging was performed.

Torsional testing of tibiae. Tests of torsional load were performed in a blinded fashion. After removal of the pins and embedding of the tibial plateau as the distal tibia, the torsional load was applied at speed of 5°/second for a maximum of 36 seconds. Maximum rotation angle at failure (Deg) and stiffness (N-cm/degree) were used as primary endpoints. Maximum torque was the highest force that the bone could sustain before fracture, and stiffness was calculated from the linear portion of the loading curve (higher values for both are indicative of stronger bone) *(17)*.

mRNA-sequencing (mRNA-seq) and analysis. mRNA sequencing data was obtained from GSE152677 *(20)*. Thirty-five femoral fractures mRNA-seq datasets were aligned to the mouse reference genome mm10. The fastq-dump files were obtained from the BioProject PRJNA640062.

bioRxiv preprint doi: https://doi.org/10.1101/2021.05.18.444618; this version posted May 19, 2021. The copyright holder for this preprint (which was not certified by peer review) is the author/funder, who has granted bioRxiv a license to display the preprint in perpetuity. It is made available under aCC-BY 4.0 International license.

Quality control of fastq files was carried out via FastQC (version 0.72) and reads were mapped to the mouse reference genome [mm10] using HISAT2 (version 2.1.0) on Galaxy (version 7). Read counts were generated using the featureCounts tool (version 2.0.1) and analyzed for differential gene expression using DESeq2 (version 2.11.40.6). Significantly differentially regulated genes were selected by a Benjamini-Hochberg adjusted p-value <0.05 and log2-fold changes above 0.5 or below -0.5. The used R-packages for the downstream analysis were PCAtools (2.2.0) and corrplot (0.84).

Single cell RNA-sequencing (scRNA-seq). Publicly available single cell RNA-seq data based on bone and bone marrow from C57BL/6J mice (n=4 each) *(26,47)* (GSE128423) were analyzed. Sequencing data were aligned to the mouse reference genome mm10 and cells with at least 500 unique molecular identifiers (UMIs), log10 genes per UMI >0.8, >250 genes per cell and a mitochondrial ratio of less than 0.2% were extracted, normalized and integrated using the Seurat package v3.0 in R 4.0.2. Subsequent R-packages were Nebulosa (3.13) and Monocle (2.18.0).

Quantitative real-time polymerase chain reaction (qRT-PCR) analysis. For callus analyses, callus and contralateral intact bone were immediately homogenized in QIAzol Lysis Reagent (QIAGEN, Valencia, CA), and stored at -80°C. Subsequent RNA extraction, cDNA synthesis, and targeted gene expression measurements of mRNA levels by qRT-PCR were performed as described previously *(48)*. Total RNA was extracted according to the manufacturer's instructions using QIAzol Lysis Reagent. Purification with RNeasy Mini Columns (QIAGEN, Valencia, CA) was subsequently performed. On-column RNase-free DNase solution (QIAGEN, Valencia, CA), was applied to degrade contaminating genomic DNA. RNA quantity was assessed with Nanodrop spectrophotometry (Thermo Fisher Scientific, Wilmington, DE). Standard reverse transcriptase was performed using High-Capacity cDNA Reverse Transcription Kit (Applied Biosystems by Life Technologies, Foster City, CA). Transcript mRNA levels were determined by qRT-PCR on the ABI Prism 7900HT Real Time System (Applied Biosystems, Carlsbad, CA), using SYBR green (Qiagen, Valencia, CA). The mouse primer sequences, designed using Primer Express Software Version 3.0 (Applied Biosystems), for the genes measured by SYBR green are provided in Supplementary Table S1. Input RNA was normalized using two reference genes (*Actb*, *Gapdh*) from which the most stable reference gene was determined by the geNorm algorithm. For each sample, the median cycle threshold (Ct) of each gene (run in triplicate) was normalized to the geometric mean of the median Ct of the most stable reference gene. The delta Ct for each gene

bioRxiv preprint doi: https://doi.org/10.1101/2021.05.18.444618; this version posted May 19, 2021. The copyright holder for this preprint (which was not certified by peer review) is the author/funder, who has granted bioRxiv a license to display the preprint in perpetuity. It is made available under aCC-BY 4.0 International license.

was used to calculate the relative mRNA expression changes for each sample. Genes with Ct values >35 were considered not expressed (NE), as done previously *(9)*.

Senescence-associated distension of satellites (SADS) analysis. Our group recently demonstrated that with fluorescence *in situ* hybridization (FISH), senescent cells display large-scale unraveling of peri-centromeric satellite heterochromatin DNA, referred to as SADS, a feature of senescent cells which has been demonstrated in osteocytes, fibroblasts, hepatocytes, glial cells and multiple other cell types *(6,5,49,50)*. As described in detail previously, SADS identification was performed on non-decalcified mouse femur sections by FISH *(4,6,5)*. After 4% paraformaldehyde (PFA) crosslinking of femur sections for 20 minutes, sections were washed three times (five minutes each in PBS), and dehydrated in ethanol (70%, 90%, 100%, each for three minutes). Sections were air dried, denatured for 10 minutes at 80°C in hybridization buffer (0.1M Tris, pH 7.2; 25mM $MgCl_2$; 70% formamide [Sigma-Aldrich, Saint Louis, MO], 5% blocking reagent [Roche] with 1.0µg/mL of Cy3-labelled (F3002) CENPB-specific [ATTCGTTGGAAACGGGA] peptide nucleic acid (PNA) probe [Panagene Inc., Korea]) and hybridized in a dark room for two hours at room temperature (RT). Subsequently, the femur sections were washed and mounted with vectashield DAPI-containing mounting media (Life Technologies). With a confocal microscope, SADS (i.e. decondensed and elongated centromeres) were visualized and quantified in a blinded fashion; a senescent cell was defined with a cut-off ≥4 SADS per cell *(5,6)*.

Western blot analysis. Protein was isolated from the pink, organic phase obtained after RNA extraction using QIAzol as previously described *(51)*. Briefly, 300 µl ethanol were added to approximately 700 µl organic phase and incubated at RT for 3 min. Upon centrifugation (2,000xg, 4°C, 5 min), the supernatant was mixed with 1.5 ml isopropanol and incubated at RT for 10 min. Samples were spun down (12,000xg, 4°C, 10 min) and the pellet was resuspended in 2 ml 0.3 M guanidine hydrochloride in 95% ethanol and kept at RT for 20 min. After centrifugation (12,000xg, 4°C, 5 min), the previous step was repeated by resuspending the pellet in 0.3 M guanidine hydrochloride, incubating at RT and spinning down the sample. This step was repeated by washing the protein pellet in ethanol and air-drying at RT for 5 min. Proteins were solubilized in 0.5 ml 1% SDS and after centrifugation (10,000xg, 4°C, 10 min), protein concentrations were determined using a Bradford assay (Bio Rad, 5000201) according to the manufacturer's instructions. 4× Laemmli buffer (Bio Rad, 161-0747) was added, samples were boiled at 95°C for 5 min and 20 µg protein/sample was separated by SDS-PAGE. Proteins were transferred onto a

bioRxiv preprint doi: https://doi.org/10.1101/2021.05.18.444618; this version posted May 19, 2021. The copyright holder for this preprint (which was not certified by peer review) is the author/funder, who has granted bioRxiv a license to display the preprint in perpetuity. It is made available under aCC-BY 4.0 International license.

PVDF membrane (0.45µm, IPVH00010, Millipore) and detected using antibodies targeting $p16^{INK4A}$ (Abcam, #ab211542, 1:1,000) and Beta-Actin (Cell Signaling, #4970, 1:1,000). After incubation with HRP-coupled secondary antibodies, proteins were visualized using a BioRad Universal Hood II Gel Documentation System.

Telomere-associated foci (TAF) analysis. To determine cellular senescence in the diaphyseal bone and callus, TAF was performed on murine left femora of non-decalcified methylmethacrylate (MMA)-embedded sections (n=4/group). Our protocol was adapted from Coppé et al. *(52)* and described before *(48)*. In brief, bone sections were de-plasticized and hydrated in EtOH gradient followed by water and PBS. Antigen was retrieved by incubation in Tris-EDTA (pH 9.0) at 95°C for 15 min. After cool-down and hydration with water and PBS (0.5% Tween-20/0.1% Triton100X), slides were placed in a blocking buffer (1:60 normal goat serum [Vector Laboratories; Cat. #S-1000] in 0.1% BSA/PBS) for 30 min at RT. The primary antibody targeting γ-H2A.X (Cell Signaling, #9718, 1:200) was diluted in blocking buffer and incubated overnight at 4°C in a humid chamber. The next day, slides were washed with 0.5% Tween-20/0.1% Triton100X in PBS followed by PBS alone, and then incubated for 30 min with secondary goat, anti-rabbit antibody biotinylated (Vector Laboratories, #BA-1000, 1:200) in blocking buffer. Afterwards, slides were washed with 0.5% Tween-20/0.1% Triton100X in PBS followed by PBS alone, and then incubated for 60 min with the tertiary antibody (Cy5 Streptavidin, Vector Laboratories, #SA-1500, 1:500) in PBS. Slides were subsequently washed three times with PBS, followed by FISH for TAF detection. Following 4% paraformaldehyde (PFA) crosslinking for 20 min, sections were washed three times (five minutes each in PBS), and dehydrated in graded ice-cold EtOH (70%, 90%, and 100% for three minutes each). Sections were dried and denatured for 10 min at 80°C in hybridization buffer (0.1M Tris, pH 7.2, 25mM MgCl2, 70% formamide [Sigma-Aldrich, Saint Louis, MO], 5% blocking reagent [Roche] with 1.0 µg/mL of Cy-3-labeled telomere-specific [CCCTAA] peptide nucleic acid [PNA] probe [TelC-Cy3, Panagene Inc., Korea; Cat. #F1002]). The slides were then hybridized in a humid chamber for two hours at RT. Sections were washed and mounted with vectashield DAPI-containing mounting media (Life Technologies) prior to image acquisition and analysis. The number of TAF per cell was quantified in a blinded fashion by examining overlap of signals from the telomere probe with γ-H2A.X. The mean number of TAF per cell in bone diaphysis and/ or callus was quantified using FIJI (Image J; NIH, Bethesda, MD, USA), and the percentage (%) of TAF-positive (TAF+) cells was calculated for each mouse based on the following criteria: % of cells with ≥1TAF, % of cells with ≥2 TAF, and % of cells with ≥3 TAF, respectively. A senescent cell was defined with a cut-off ≥3 TAF per cell *(34)*.

bioRxiv preprint doi: https://doi.org/10.1101/2021.05.18.444618; this version posted May 19, 2021. The copyright holder for this preprint (which was not certified by peer review) is the author/funder, who has granted bioRxiv a license to display the preprint in perpetuity. It is made available under aCC-BY 4.0 International license.

Cell culture experiments. Metaphyses were cut in the right tibia, both femora and both humeri to flush the bone marrow and culture bone marrow MSCs in 75ml flasks at 37°C and 5% CO2 in growth medium (DMEM, 15% FBS, 1% Glutamax (100x), 1% Anti/Anti (100x), 0.5% Gentamicin). The medium was changed every other day and cells were plated onto 24- or 96-well plates for functional characterization assays. Senescence was induced by treating cells with 100 µM H2O2 for four hours *(53–57)*. *In vitro* senolytics treatment was performed by incubating cells with 200 nM Dasatinib and 50 µM Quercetin or DMSO as vehicle for 24 hours as described elsewhere *(44)*.

SA-β-Gal staining. To assess senescence *in vitro*, cellular SA-β-Gal activity was measured as described previously *(14)*. After BMSCs were washed in PBS (pH 7.4) and fixed with 2% formaldehyde (Sigma-Aldrich) and 25% glutaraldehyde (Sigma-Aldrich) for 5 minutes, they were washed three times using PBS. Cells were then incubated in SA-β-Gal solution (1 mg/ml X-Gal, 40 mM citric acid, pH 6.0, 5 mM potassium ferrocyanide, 5 mM potassium ferricyanide, 150 mM NaCl, 2 mM $MgCl_2$) at 37°C for 16 hours. Cells were washed in ice-cold PBS and stored in PBS at 37°C until analysis. DAPI (Life Technologies) was used to stain nuclei for cell counting. In blinded fashion, ten images per well were taken from random fields using fluorescence microscopy (Nikon Eclipse Ti). Total cell numbers were determined automatically (IX Pico, Molecular Devices, processed using the CellReporterXpress® software) and visualized using crystal violet. For this purpose, cells were fixed in 4% formaldehyde in PBS for 20 min and, upon washing with PBS, stained with 1% (w/v) crystal violet in 20% ethanol for 20 minutes. Excess dye was removed and upon drying, images were acquired.

Statistics. Graphical data are shown as Means ± standard error of the mean (SEM) unless otherwise specified. The sample sizes were determined based on previously conducted and published experiments (e.g. *(6,9)*) in which statistically significant differences were observed among various bone parameters in response to multiple interventions in our laboratory. The used animal numbers are indicated in the Figure Legends; all samples presented represent biological replicates. No mice, samples, or data points were excluded from analyses. Data were examined for normality and distribution using dot plots and histograms; all variables were examined for skewness and kurtosis. If the normality or equal variance assumptions for parametric analysis methods were not met, data were analyzed using non-parametric tests (e.g., Wilcoxon Rank Sum test, Mann-Whitney U test). For parametric tests, depending on the comparison, differences

bioRxiv preprint doi: https://doi.org/10.1101/2021.05.18.444618; this version posted May 19, 2021. The copyright holder for this preprint (which was not certified by peer review) is the author/funder, who has granted bioRxiv a license to display the preprint in perpetuity. It is made available under aCC-BY 4.0 International license.

between groups were analyzed by independent samples t-test or one-way ANOVA, where justified as appropriate. When ANOVA determined a statistically significant ($p<0.05$) effect, pairwise multiple comparisons were performed and the Tukey post-hoc method was applied. Statistical analyses were performed using either GraphPad Prism (Version 9.0) or R version 4.0.2. A p-value <0.05 (two-tailed) was considered statistically significant.

Study approval. Animal studies were performed under protocols approved by the Institutional Animal Care and Use Committee (IACUC), and experiments were performed in accordance with Mayo Clinic IACUC guidelines.

Author contributions. S.K., J.N.F., D.G.M., and D.S. conceived and directed the project. J.N.F. and D.S. designed the experiments and interpreted the data with input from S.K. Experiments were performed by D.S., J.L.R., D.G.F., R.L.K. and J.N.F. D.S., R.L.K. and J.N.F. wrote the manuscript. All authors reviewed the manuscript. J.N.F. and S.K. oversaw all experimental design, data analyses, and manuscript preparation. J.N.F., S.K., and D.S. accept responsibility for the integrity of the data analysis.

Acknowledgements. This work was supported by the German Research Foundation (DFG, 413501650) (D.S.), National Institutes of Health (NIH) grants P01 AG062413 (S.K., J.N.F.), R21 AG065868 (S.K., J.N.F), K01 AR070241 (J.N.F.), R01 AG063707 (D.G.M.), and Mildred Scheel postdoc fellowship by the German Cancer Aid (R.L.K.).

Competing interests. The authors report no financial or non-financial competing interests.

bioRxiv preprint doi: https://doi.org/10.1101/2021.05.18.444618; this version posted May 19, 2021. The copyright holder for this preprint (which was not certified by peer review) is the author/funder, who has granted bioRxiv a license to display the preprint in perpetuity. It is made available under aCC-BY 4.0 International license.

References

1. Khosla, S., Farr, J. N., Tchkonia, T., and Kirkland, J. L. (2020) The role of cellular senescence in ageing and endocrine disease, *Nature reviews. Endocrinology 16,* 263–275.

2. López-Otín, C., Blasco, M. A., Partridge, L., Serrano, M., and Kroemer, G. (2013) The hallmarks of aging, *Cell 153,* 1194–1217.

3. Chandra, A., Lagnado, A. B., Farr, J. N., Monroe, D. G., Park, S., Hachfeld, C., Tchkonia, T., Kirkland, J. L., Khosla, S., Passos, J. F., and Pignolo, R. J. (2020) Targeted Reduction of Senescent Cell Burden Alleviates Focal Radiotherapy-Related Bone Loss, *Journal of bone and mineral research : the official journal of the American Society for Bone and Mineral Research 35,* 1119–1131.

4. Farr, J. N., and Khosla, S. (2019) Cellular senescence in bone, *Bone 121,* 121–133.

5. Farr, J. N., Rowsey, J. L., Eckhardt, B. A., Thicke, B. S., Fraser, D. G., Tchkonia, T., Kirkland, J. L., Monroe, D. G., and Khosla, S. (2019) Independent Roles of Estrogen Deficiency and Cellular Senescence in the Pathogenesis of Osteoporosis: Evidence in Young Adult Mice and Older Humans, *Journal of bone and mineral research : the official journal of the American Society for Bone and Mineral Research 34,* 1407–1418.

6. Farr, J. N., Xu, M., Weivoda, M. M., Monroe, D. G., Fraser, D. G., Onken, J. L., Negley, B. A., Sfeir, J. G., Ogrodnik, M. B., Hachfeld, C. M., LeBrasseur, N. K., Drake, M. T., Pignolo, R. J., Pirtskhalava, T., Tchkonia, T., Oursler, M. J., Kirkland, J. L., and Khosla, S. (2017) Targeting cellular senescence prevents age-related bone loss in mice, *Nature medicine 23,* 1072–1079.

7. Khosla, S., Farr, J. N., and Kirkland, J. L. (2018) Inhibiting Cellular Senescence: A New Therapeutic Paradigm for Age-Related Osteoporosis, *The Journal of clinical endocrinology and metabolism 103,* 1282–1290.

8. Xu, M., Pirtskhalava, T., Farr, J. N., Weigand, B. M., Palmer, A. K., Weivoda, M. M., Inman, C. L., Ogrodnik, M. B., Hachfeld, C. M., Fraser, D. G., Onken, J. L., Johnson, K. O., Verzosa, G. C., Langhi, L. G. P., Weigl, M., Giorgadze, N., LeBrasseur, N. K., Miller, J. D., Jurk, D., Singh, R. J., Allison, D. B., Ejima, K., Hubbard, G. B., Ikeno, Y., Cubro, H., Garovic, V. D., Hou, X., Weroha, S. J., Robbins, P. D., Niedernhofer, L. J., Khosla, S., Tchkonia, T., and Kirkland, J. L. (2018) Senolytics improve physical function and increase lifespan in old age, *Nature medicine 24,* 1246–1256.

9. Farr, J. N., Fraser, D. G., Wang, H., Jaehn, K., Ogrodnik, M. B., Weivoda, M. M., Drake, M. T., Tchkonia, T., LeBrasseur, N. K., Kirkland, J. L., Bonewald, L. F., Pignolo, R. J., Monroe, D. G., and Khosla, S. (2016) Identification of Senescent Cells in the Bone Microenvironment, *Journal of bone and mineral research : the official journal of the American Society for Bone and Mineral Research 31,* 1920–1929.

10. Tchkonia, T., Zhu, Y., van Deursen, J., Campisi, J., and Kirkland, J. L. (2013) Cellular senescence and the senescent secretory phenotype: therapeutic opportunities, *The Journal of clinical investigation 123,* 966–972.

11. Lagnado, A., Leslie, J., Ruchaud-Sparagano, M.-H., Victorelli, S., Hirsova, P., Ogrodnik, M., Collins, A. L., Vizioli, M. G., Habiballa, L., Saretzki, G., Evans, S. A., Salmonowicz, H., Hruby, A., Geh, D., Pavelko, K. D., Dolan, D., Reeves, H. L., Grellscheid, S., Wilson, C. H., Pandanaboyana, S., Doolittle, M., Zglinicki, T. von, Oakley, F., Gallage, S., Wilson, C. L., Birch, J., Carroll, B., Chapman, J., Heikenwalder, M., Neretti, N., Khosla, S., Masuda, C. A., Tchkonia, T., Kirkland, J. L., Jurk, D., Mann,

bioRxiv preprint doi: https://doi.org/10.1101/2021.05.18.444618; this version posted May 19, 2021. The copyright holder for this preprint (which was not certified by peer review) is the author/funder, who has granted bioRxiv a license to display the preprint in perpetuity. It is made available under aCC-BY 4.0 International license.

754 D. A., and Passos, J. F. (2021) Neutrophils induce paracrine telomere dysfunction and senescence in
755 ROS-dependent manner, *The EMBO journal*, e106048.

756 12. Nelson, G., Wordsworth, J., Wang, C., Jurk, D., Lawless, C., Martin-Ruiz, C., and Zglinicki, T. von
757 (2012) A senescent cell bystander effect: senescence-induced senescence, *Aging cell 11*, 345–349.

758 13. Xu, M., Palmer, A. K., Ding, H., Weivoda, M. M., Pirtskhalava, T., White, T. A., Sepe, A., Johnson,
759 K. O., Stout, M. B., Giorgadze, N., Jensen, M. D., LeBrasseur, N. K., Tchkonia, T., and Kirkland, J. L.
760 (2015) Targeting senescent cells enhances adipogenesis and metabolic function in old age, *eLife* Epub
761 2015. DOI: 10.7554/eLife.12997.

762 14. Xu, M., Tchkonia, T., Ding, H., Ogrodnik, M., Lubbers, E. R., Pirtskhalava, T., White, T. A.,
763 Johnson, K. O., Stout, M. B., Mezera, V., Giorgadze, N., Jensen, M. D., LeBrasseur, N. K., and Kirkland,
764 J. L. (2015) JAK inhibition alleviates the cellular senescence-associated secretory phenotype and frailty in
765 old age, *Proceedings of the National Academy of Sciences of the United States of America 112*, E6301-10.

766 15. Demaria, M., Ohtani, N., Youssef, S. A., Rodier, F., Toussaint, W., Mitchell, J. R., Laberge, R.-M.,
767 Vijg, J., van Steeg, H., Dollé, M. E., Hoeijmakers, J. H., Bruin, A. de, Hara, E., and Campisi, J. (2014)
768 An Essential Role for Senescent Cells in Optimal Wound Healing through Secretion of PDGF-AA,
769 *Developmental cell 31*, 722–733.

770 16. Marsell, R., and Einhorn, T. A. (2011) THE BIOLOGY OF FRACTURE HEALING, *Injury 42*, 551–
771 555.

772 17. Undale, A., Fraser, D., Hefferan, T., Kopher, R. A., Herrick, J., Evans, G. L., Li, X., Kakar, S., Hayes,
773 M., Atkinson, E., Yaszemski, M. J., Kaufman, D. S., Westendorf, J. J., and Khosla, S. (2011) Induction of
774 fracture repair by mesenchymal cells derived from human embryonic stem cells or bone marrow, *Journal*
775 *of orthopaedic research : official publication of the Orthopaedic Research Society 29*, 1804–1811.

776 18. Saul, D., Weber, M., Zimmermann, M. H., Kosinsky, R. L., Hoffmann, D. B., Menger, B., Taudien,
777 S., Lehmann, W., Komrakova, M., and Sehmisch, S. (2019) Effect of the lipoxygenase inhibitor baicalein
778 on bone tissue and bone healing in ovariectomized rats, *Nutrition & metabolism 16*, 4.

779 19. Burd, C. E., Sorrentino, J. A., Clark, K. S., Darr, D. B., Krishnamurthy, J., Deal, A. M., Bardeesy, N.,
780 Castrillon, D. H., Beach, D. H., and Sharpless, N. E. (2013) Monitoring tumorigenesis and senescence in
781 vivo with a p16(INK4a)-luciferase model, *Cell 152*, 340–351.

782 20. Coates, B. A., McKenzie, J. A., Buettmann, E. G., Liu, X., Gontarz, P. M., Zhang, B., and Silva, M. J.
783 (2019) Transcriptional profiling of intramembranous and endochondral ossification after fracture in mice,
784 *Bone 127*, 577–591.

785 21. Supek, F., Bošnjak, M., Škunca, N., and Šmuc, T. (2011) REVIGO summarizes and visualizes long
786 lists of gene ontology terms, *PloS one 6*, e21800.

787 22. Farr, J. N., and Almeida, M. (2018) The Spectrum of Fundamental Basic Science Discoveries
788 Contributing to Organismal Aging, *Journal of bone and mineral research : the official journal of the*
789 *American Society for Bone and Mineral Research 33*, 1568–1584.

790 23. Wehrle, E., Tourolle Né Betts, D. C., Kuhn, G. A., Scheuren, A. C., Hofmann, S., and Müller, R.
791 (2019) Evaluation of longitudinal time-lapsed in vivo micro-CT for monitoring fracture healing in mouse
792 femur defect models, *Scientific reports 9*, 17445.

793 24. Jurk, D., Wilson, C., Passos, J. F., Oakley, F., Correia-Melo, C., Greaves, L., Saretzki, G., Fox, C.,
794 Lawless, C., Anderson, R., Hewitt, G., Pender, S. L., Fullard, N., Nelson, G., Mann, J., van de Sluis, B.,

bioRxiv preprint doi: https://doi.org/10.1101/2021.05.18.444618; this version posted May 19, 2021. The copyright holder for this preprint (which was not certified by peer review) is the author/funder, who has granted bioRxiv a license to display the preprint in perpetuity. It is made available under aCC-BY 4.0 International license.

795 Mann, D. A., and Zglinicki, T. von (2014) Chronic inflammation induces telomere dysfunction and
796 accelerates ageing in mice, *Nature communications 2,* 4172.

797 25. Schafer, M. J., Haak, A. J., Tschumperlin, D. J., and LeBrasseur, N. K. (2018) Targeting Senescent
798 Cells in Fibrosis: Pathology, Paradox, and Practical Considerations, *Current rheumatology reports 20,* 3.

799 26. Baryawno, N., Przybylski, D., Kowalczyk, M. S., Kfoury, Y., Severe, N., Gustafsson, K., Kokkaliaris,
800 K. D., Mercier, F., Tabaka, M., Hofree, M., Dionne, D., Papazian, A., Lee, D., Ashenberg, O.,
801 Subramanian, A., Vaishnav, E. D., Rozenblatt-Rosen, O., Regev, A., and Scadden, D. T. (2019) A
802 Cellular Taxonomy of the Bone Marrow Stroma in Homeostasis and Leukemia, *Cell 177,* 1915-1932.e16.

803 27. Baker, D. J., Wijshake, T., Tchkonia, T., LeBrasseur, N. K., Childs, B. G., van de Sluis, B., Kirkland,
804 J. L., and van Deursen, J. M. (2011) Clearance of p16Ink4a-positive senescent cells delays ageing-
805 associated disorders, *Nature 479,* 232–236.

806 28. Palmer, A. K., Tchkonia, T., and Kirkland, J. L. (2021) Senolytics: Potential for Alleviating Diabetes
807 and Its Complications, *Endocrinology* Epub 2021. DOI: 10.1210/endocr/bqab058.

808 29. Tchkonia, T., Palmer, A. K., and Kirkland, J. L. (2021) New Horizons: Novel Approaches to Enhance
809 Healthspan Through Targeting Cellular Senescence and Related Aging Mechanisms, *The Journal of*
810 *clinical endocrinology and metabolism 106,* e1481-e1487.

811 30. Braun, H., Schmidt, B. M. W., Raiss, M., Baisantry, A., Mircea-Constantin, D., Wang, S., Gross, M.-
812 L., Serrano, M., Schmitt, R., and Melk, A. (2012) Cellular senescence limits regenerative capacity and
813 allograft survival, *Journal of the American Society of Nephrology : JASN 23,* 1467–1473.

814 31. Saul, D., and Kosinsky, R. L. (2021) Epigenetics of Aging and Aging-Associated Diseases,
815 *International journal of molecular sciences* Epub 2021. DOI: 10.3390/ijms22010401.

816 32. Kowald, A., Passos, J. F., and Kirkwood, T. B. L. (2020) On the evolution of cellular senescence,
817 *Aging cell 19,* e13270.

818 33. Hewitt, G., Jurk, D., Marques, F. D. M., Correia-Melo, C., Hardy, T., Gackowska, A., Anderson, R.,
819 Taschuk, M., Mann, J., and Passos, J. F. (2012) Telomeres are favoured targets of a persistent DNA
820 damage response in ageing and stress-induced senescence, *Nature communications 3,* 708.

821 34. Anderson, R., Lagnado, A., Maggiorani, D., Walaszczyk, A., Dookun, E., Chapman, J., Birch, J.,
822 Salmonowicz, H., Ogrodnik, M., Jurk, D., Proctor, C., Correia-Melo, C., Victorelli, S., Fielder, E.,
823 Berlinguer-Palmini, R., Owens, A., Greaves, L. C., Kolsky, K. L., Parini, A., Douin-Echinard, V.,
824 LeBrasseur, N. K., Arthur, H. M., Tual-Chalot, S., Schafer, M. J., Roos, C. M., Miller, J. D., Robertson,
825 N., Mann, J., Adams, P. D., Tchkonia, T., Kirkland, J. L., Mialet-Perez, J., Richardson, G. D., and Passos,
826 J. F. (2019) Length-independent telomere damage drives post-mitotic cardiomyocyte senescence, *The*
827 *EMBO journal* Epub 2019. DOI: 10.15252/embj.2018100492.

828 35. Millerand, M., Berenbaum, F., and Jacques, C. (2019) Danger signals and inflammaging in
829 osteoarthritis, *Clinical and experimental rheumatology 37 Suppl 120,* 48–56.

830 36. Yao, Z., Murali, B., Ren, Q., Luo, X., Faget, D. V., Cole, T., Ricci, B., Thotala, D., Monahan, J., van
831 Deursen, J. M., Baker, D., Faccio, R., Schwarz, J. K., and Stewart, S. A. (2020) Therapy-Induced
832 Senescence Drives Bone Loss, *Cancer research 80,* 1171–1182.

833 37. Acosta, J. C., Banito, A., Wuestefeld, T., Georgilis, A., Janich, P., Morton, J. P., Athineos, D., Kang,
834 T.-W., Lasitschka, F., Andrulis, M., Pascual, G., Morris, K. J., Khan, S., Jin, H., Dharmalingam, G.,
835 Snijders, A. P., Carroll, T., Capper, D., Pritchard, C., Inman, G. J., Longerich, T., Sansom, O. J., Benitah,

bioRxiv preprint doi: https://doi.org/10.1101/2021.05.18.444618; this version posted May 19, 2021. The copyright holder for this preprint (which was not certified by peer review) is the author/funder, who has granted bioRxiv a license to display the preprint in perpetuity. It is made available under aCC-BY 4.0 International license.

836 S. A., Zender, L., and Gil, J. (2013) A complex secretory program orchestrated by the inflammasome
837 controls paracrine senescence, *Nature cell biology 15*, 978–990.
838 38. Basisty, N., Kale, A., Jeon, O. H., Kuehnemann, C., Payne, T., Rao, C., Holtz, A., Shah, S., Sharma,
839 V., Ferrucci, L., Campisi, J., and Schilling, B. (2020) A proteomic atlas of senescence-associated
840 secretomes for aging biomarker development, *PLoS biology 18*, e3000599.
841 39. Coppé, J.-P., Desprez, P.-Y., Krtolica, A., and Campisi, J. (2010) The senescence-associated secretory
842 phenotype: the dark side of tumor suppression, *Annual review of pathology 5*, 99–118.
843 40. Özcan, S., Alessio, N., Acar, M. B., Mert, E., Omerli, F., Peluso, G., and Galderisi, U. (2016)
844 Unbiased analysis of senescence associated secretory phenotype (SASP) to identify common components
845 following different genotoxic stresses, *Aging 8*, 1316–1329.
846 41. Magalhães, J. P. de, and Passos, J. F. (2018) Stress, cell senescence and organismal ageing,
847 *Mechanisms of ageing and development 170*, 2–9.
848 42. Pratsinis, H., Mavrogonatou, E., and Kletsas, D. (2019) Scarless wound healing: From development to
849 senescence, *Advanced drug delivery reviews 146*, 325–343.
850 43. Wilkinson, H. N., and Hardman, M. J. (2020) Senescence in Wound Repair: Emerging Strategies to
851 Target Chronic Healing Wounds, *Frontiers in cell and developmental biology 8*, 773.
852 44. Zhu, Y., Tchkonia, T., Pirtskhalava, T., Gower, A. C., Ding, H., Giorgadze, N., Palmer, A. K., Ikeno,
853 Y., Hubbard, G. B., Lenburg, M., O'Hara, S. P., LaRusso, N. F., Miller, J. D., Roos, C. M., Verzosa, G.
854 C., LeBrasseur, N. K., Wren, J. D., Farr, J. N., Khosla, S., Stout, M. B., McGowan, S. J., Fuhrmann-
855 Stroissnigg, H., Gurkar, A. U., Zhao, J., Colangelo, D., Dorronsoro, A., Ling, Y. Y., Barghouthy, A. S.,
856 Navarro, D. C., Sano, T., Robbins, P. D., Niedernhofer, L. J., and Kirkland, J. L. (2015) The Achilles'
857 heel of senescent cells: from transcriptome to senolytic drugs, *Aging cell 14*, 644–658.
858 45. Wang, C., Inzana, J. A., Mirando, A. J., Ren, Y., Liu, Z., Shen, J., O'Keefe, R. J., Awad, H. A., and
859 Hilton, M. J. (2016) NOTCH signaling in skeletal progenitors is critical for fracture repair, *The Journal of*
860 *clinical investigation 126*, 1471–1481.
861 46. Liu, Y.-Z., Akhter, M. P., Gao, X., Wang, X.-Y., Wang, X.-B., Zhao, G., Wei, X., Wu, H.-J., Chen,
862 H., Wang, D., and Cui, L. (2018) Glucocorticoid-induced delayed fracture healing and impaired bone
863 biomechanical properties in mice, *Clinical interventions in aging 13*, 1465–1474.
864 47. van Gastel, N., Stegen, S., Eelen, G., Schoors, S., Carlier, A., Daniëls, V. W., Baryawno, N.,
865 Przybylski, D., Depypere, M., Stiers, P.-J., Lambrechts, D., van Looveren, R., Torrekens, S., Sharda, A.,
866 Agostinis, P., Lambrechts, D., Maes, F., Swinnen, J. V., Geris, L., van Oosterwyck, H., Thienpont, B.,
867 Carmeliet, P., Scadden, D. T., and Carmeliet, G. (2020) Lipid availability determines fate of skeletal
868 progenitor cells via SOX9, *Nature 579*, 111–117.
869 48. Eckhardt, B. A., Rowsey, J. L., Thicke, B. S., Fraser, D. G., O'Grady, K. L., Bondar, O. P., Hines, J.
870 M., Singh, R. J., Thoreson, A. R., Rakshit, K., Lagnado, A. B., Passos, J. F., Vella, A., Matveyenko, A.
871 V., Khosla, S., Monroe, D. G., and Farr, J. N. (2020) Accelerated osteocyte senescence and skeletal
872 fragility in mice with type 2 diabetes, *JCI insight* Epub 2020. DOI: 10.1172/jci.insight.135236.
873 49. Swanson, E. C., Manning, B., Zhang, H., and Lawrence, J. B. (2013) Higher-order unfolding of
874 satellite heterochromatin is a consistent and early event in cell senescence, *The Journal of cell biology*
875 *203*, 929–942.

bioRxiv preprint doi: https://doi.org/10.1101/2021.05.18.444618; this version posted May 19, 2021. The copyright holder for this preprint (which was not certified by peer review) is the author/funder, who has granted bioRxiv a license to display the preprint in perpetuity. It is made available under aCC-BY 4.0 International license.

50. Ogrodnik, M., Zhu, Y., Langhi, L. G. P., Tchkonia, T., Krüger, P., Fielder, E., Victorelli, S., Ruswhandi, R. A., Giorgadze, N., Pirtskhalava, T., Podgorni, O., Enikolopov, G., Johnson, K. O., Xu, M., Inman, C., Palmer, A. K., Schafer, M., Weigl, M., Ikeno, Y., Burns, T. C., Passos, J. F., Zglinicki, T. von, Kirkland, J. L., and Jurk, D. (2019) Obesity-Induced Cellular Senescence Drives Anxiety and Impairs Neurogenesis, *Cell metabolism 29*, 1061-1077.e8.

51. Hummon, A. B., Lim, S. R., Difilippantonio, M. J., and Ried, T. (2007) Isolation and solubilization of proteins after TRIzol extraction of RNA and DNA from patient material following prolonged storage, *BioTechniques 42*, 467-70, 472.

52. Coppé, J.-P., Patil, C. K., Rodier, F., Sun, Y., Muñoz, D. P., Goldstein, J., Nelson, P. S., Desprez, P.-Y., and Campisi, J. (2008) Senescence-associated secretory phenotypes reveal cell-nonautonomous functions of oncogenic RAS and the p53 tumor suppressor, *PLoS biology 6*, 2853–2868.

53. Dasari, A., Bartholomew, J. N., Volonte, D., and Galbiati, F. (2006) Oxidative Stress Induces Premature Senescence by Stimulating Caveolin-1 Gene Transcription through p38 Mitogen-Activated Protein Kinase/Sp1–Mediated Activation of Two GC-Rich Promoter Elements, *Cancer research 66*, 10805–10814.

54. Duan, J., Duan, J., Zhang, Z., and Tong, T. (2005) Irreversible cellular senescence induced by prolonged exposure to H2O2 involves DNA-damage-and-repair genes and telomere shortening, *The international journal of biochemistry & cell biology 37*, 1407–1420.

55. Kornienko, J. S., Smirnova, I. S., Pugovkina, N. A., Ivanova, J. S., Shilina, M. A., Grinchuk, T. M., Shatrova, A. N., Aksenov, N. D., Zenin, V. V., Nikolsky, N. N., and Lyublinskaya, O. G. (2019) High doses of synthetic antioxidants induce premature senescence in cultivated mesenchymal stem cells, *Scientific reports 9*, 1296.

56. Park, S. Y., Jeong, A.-J., Kim, G.-Y., Jo, A., Lee, J. E., Leem, S.-H., Yoon, J.-H., Ye, S. K., and Chung, J. W. (2017) Lactoferrin Protects Human Mesenchymal Stem Cells from Oxidative Stress-Induced Senescence and Apoptosis, *Journal of microbiology and biotechnology 27*, 1877–1884.

57. Xu, M., Su, X., Xiao, X., Yu, H., Li, X., Keating, A., Wang, S., and Zhao, R. C. (2021) Hydrogen Peroxide-Induced Senescence Reduces the Wound Healing-Promoting Effects of Mesenchymal Stem Cell-Derived Exosomes Partially via miR-146a, *Aging and disease 12*, 102–115.

58. Butler, A., Hoffman, P., Smibert, P., Papalexi, E., and Satija, R. (2018) Integrating single-cell transcriptomic data across different conditions, technologies, and species, *Nature biotechnology 36*, 411–420.

59. Alquicira-Hernandez, J., and Powell, J. E. (2021) Nebulosa recovers single cell gene expression signals by kernel density estimation, *Bioinformatics (Oxford, England)* Epub 2021. DOI: 10.1093/bioinformatics/btab003.

bioRxiv preprint doi: https://doi.org/10.1101/2021.05.18.444618; this version posted May 19, 2021. The copyright holder for this preprint (which was not certified by peer review) is the author/funder, who has granted bioRxiv a license to display the preprint in perpetuity. It is made available under aCC-BY 4.0 International license.

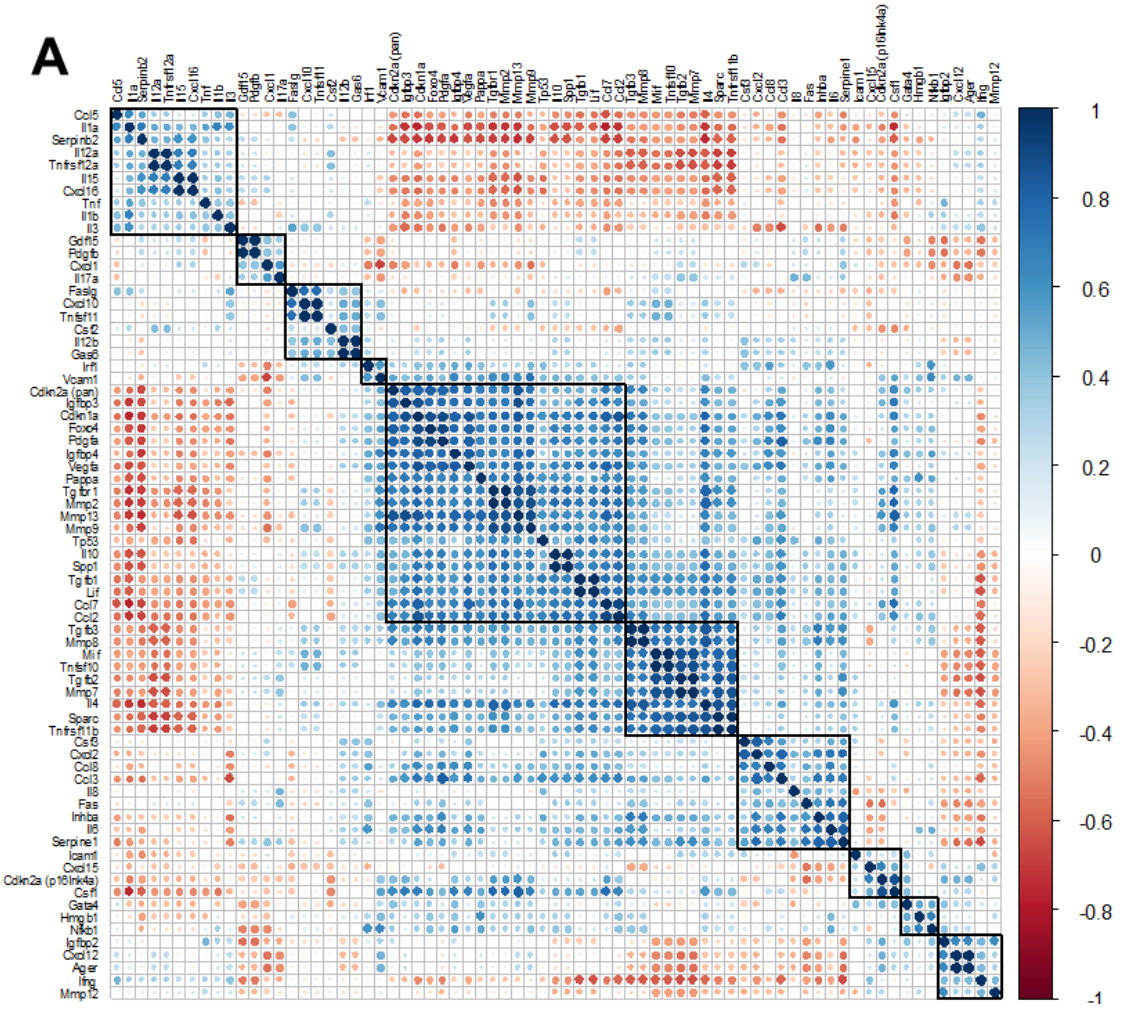

Supplementary Figure S1: (A) All SASP-associated genes and the two senescence key regulators *p16*^{Ink4a} and *p21*^{Cip1} are displayed. The color of each dot and its size represent the correlation coefficient (blue: positively regulated, red: negatively regulated). Automated clustering led to ten clusters, out of which the largest central cluster was depicted in Figure 4G.

bioRxiv preprint doi: https://doi.org/10.1101/2021.05.18.444618; this version posted May 19, 2021. The copyright holder for this preprint (which was not certified by peer review) is the author/funder, who has granted bioRxiv a license to display the preprint in perpetuity. It is made available under aCC-BY 4.0 International license.

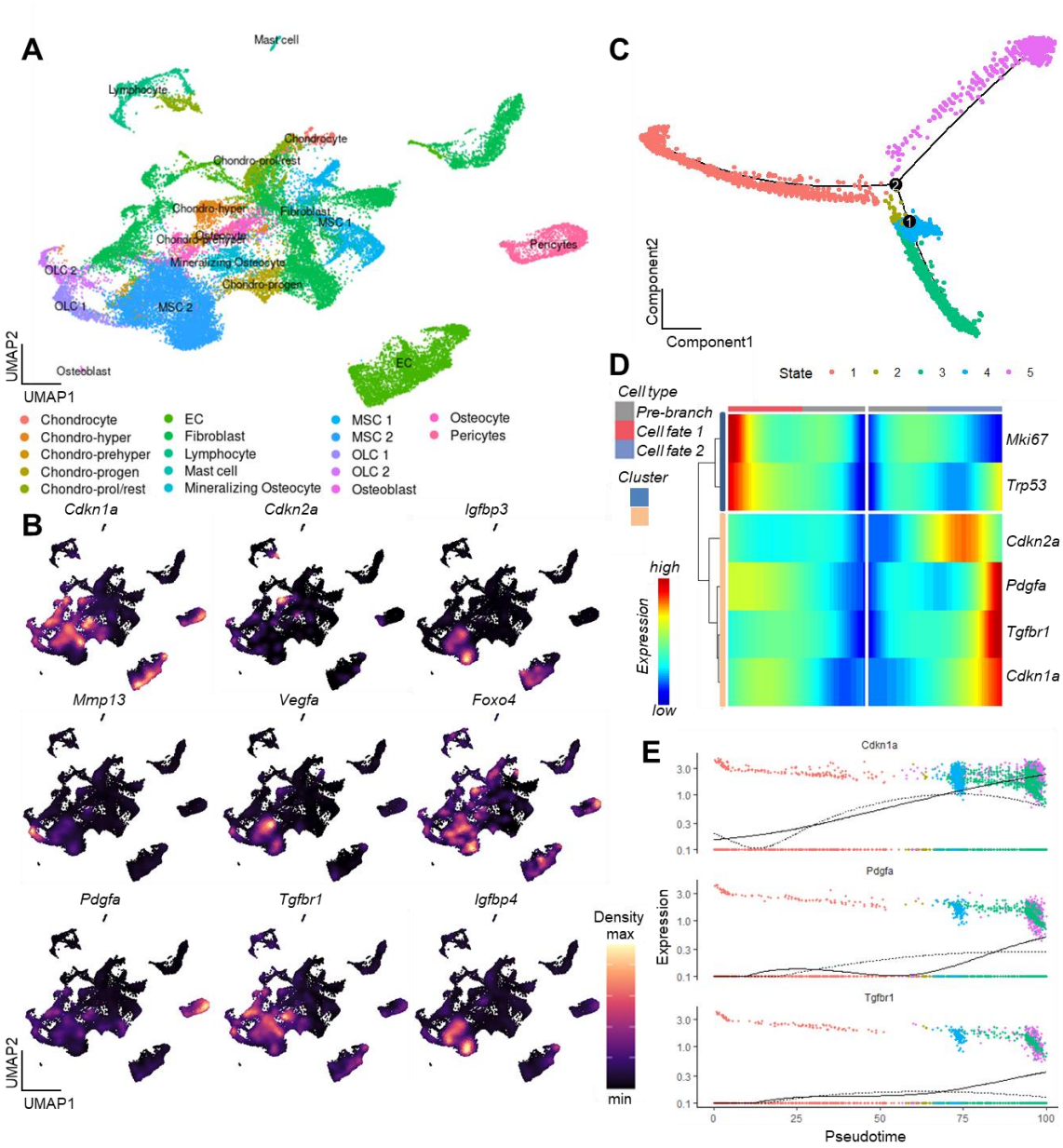

Supplementary Figure S2: (A) A Uniform Manifold Approximation and Projection (UMAP) representation of murine bone and bone marrow (*(26)*, GSE128423), after unsupervised clustering using the Seurat package *(58)*. Distinct cellular populations were clustered based on their expression patterns. (B) Applying the expression pattern of the experimentally verified central senescence-associated and SASP genes, the highest overlap was found within the MSC cluster. The density of each population's expression is estimated using Kernel Gene-Weighted Density with Nebulosa *(59)* (C) Pseudotime of MSCs showed divergent cell fates (branch point 2), out of which (D) one fate is characterized by increased *Pdgfa*, *Tgfbr1* and $p21^{Cip1}$ and reduction of *Mki67*, pointing at a senescent state. (E) The longitudinal pseudotime expression pattern depicts a marked increase of $p21^{Cip1}$ in the late cellular fate along with certain SASP markers like *Pdgfa* and *Tgfbr1*.

bioRxiv preprint doi: https://doi.org/10.1101/2021.05.18.444618; this version posted May 19, 2021. The copyright holder for this preprint (which was not certified by peer review) is the author/funder, who has granted bioRxiv a license to display the preprint in perpetuity. It is made available under aCC-BY 4.0 International license.

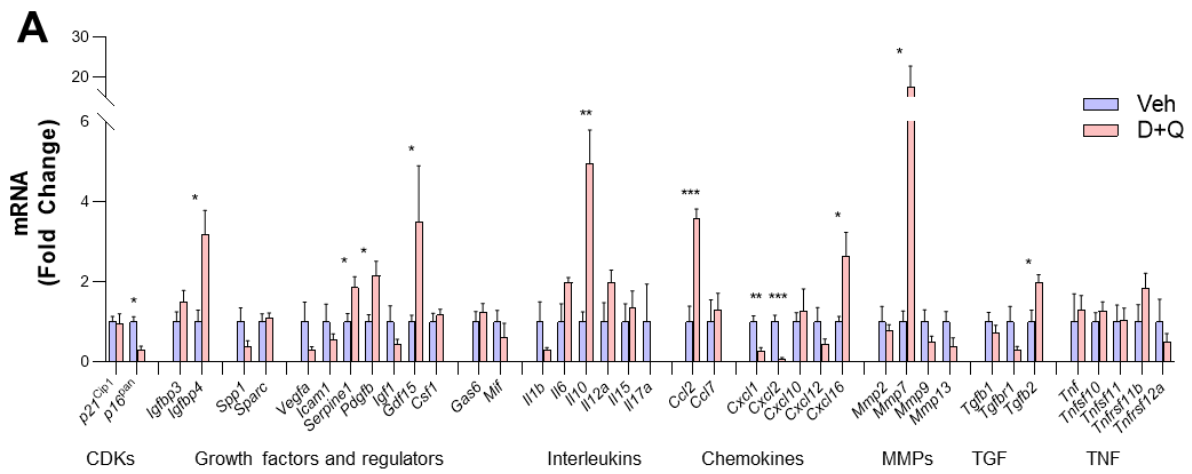

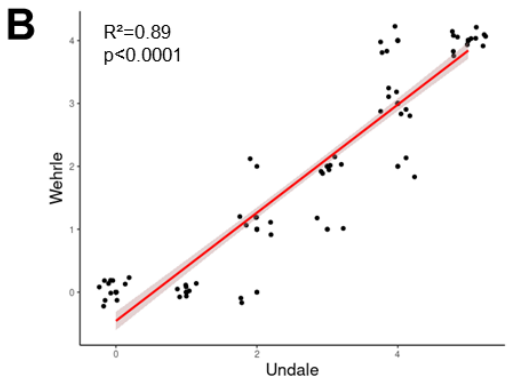

Supplementary Figure S3: (A) Changes after D+Q treatment on day 14 compared to vehicle treatment. Among the two Cyclin-dependent kinases (CDKs), *p16*^{Pan}, like p16^{Ink4a} (Figure. 6B) was significantly downregulated after D+Q treatment. Among growth factors, *Igfbp4*, *Serpine1*, *Pdgfb* and *Gdf15* were significantly upregulated, indicating higher proliferative potential. In the interleukin panel, *Il10* displayed a significantly higher expression after D+Q treatment. The chemokines *Ccl2* and *Cxcl16* showed a substantial increase, while *Cxcl1* and *Cxcl2* were significantly downregulated. *Mmp9* were substantially (17-fold) increased after treatment with D+Q, while *Tgfb2* was the only TGF-associated gene with a significant upregulation. (B) Correlation of Undale and Wehrle scores of X-ray analyses. The two fracture healing courses show reliable agreement (R^2=0.89, p<0.0001). Mean ± SEM. Mann-Whitney U test or Student's *t*-test for pairwise comparisons; p>0.05, *p<0.05, **p<0.01, ***p<0.001, ****p<0.0001.

bioRxiv preprint doi: https://doi.org/10.1101/2021.05.18.444618; this version posted May 19, 2021. The copyright holder for this preprint (which was not certified by peer review) is the author/funder, who has granted bioRxiv a license to display the preprint in perpetuity. It is made available under aCC-BY 4.0 International license.

942 Supplementary. Table S1. Mouse primer sequences

Category	Gene	Forward Primer sequence (5'-3')	Reverse Primer Sequence (5'-3')
Senescence	*p16*^{Ink4a}	GAACTCTTTCGGTCGTACCC	AGTTCGAATCTGCACCGTAGT
Senescence	*p16*^{pan}	AGCTCTTCTGCTCAACTACGG	GGAGAAGGTAGTGGGGTCCT
Senescence	*p21*^{Cip1}	GAACATCTCAGGGCCGAAAA	TGCGCTTGGAGTGATAGAAATC
Senescence	*Tp53*	TCTTATCCGGGTGGAAGGAAA	GGCGAAAAGTCTGCCTGTCTT
SASP	*Actb*	AATCGTGCGTGACATCAAAGAG	GCCATCTCCTGCTCGAAGTC
SASP	*Ager*	CTGGCACTTAGATGGGAAACT	TGTCTCCTGGTCTCTTCCTT
SASP	*Ccl2*	GTCTGTGCTGACCCCAAGAAG	TGGTTCCGATCCAGGTTTTTA
SASP	*Ccl3*	TCCCAGCCAGGTGTCATTTT	TTGGAGTCAGCGCAGATCTG
SASP	*Ccl5*	GCCCACGTCAAGGAGTATTTCT	ACAAACACGACTGCAAGATTGG
SASP	*Ccl7*	CCCTGGGAAGCTGTTATCTTCA	CTGATGGGCTTCAGCACAGA
SASP	*Ccl8*	CCACACAGAAGTGGGTCAGTGA	TTCAAGGCTGCAGAATTTGAGA
SASP	*Csf1*	ATTGCCAAGGAGGTGTCAGAA	GGACCTTCAGGTGTCCATTCC
SASP	*Csf2*	CCTTGAACATGACAGCCAGCTA	CACAGTCCGTTTCCGGAGTT
SASP	*Csf3*	CCTGCAGGCTCTATCGGGTAT	ATCCAGCTGAAGCAAGTCCAA
SASP	*Cxcl1*	CCGAAGTCATAGCCACACTCAA	CAAGGGAGCTTCAGGGTCAAG
SASP	*Cxcl10*	TGAATCCGGAATCTAAGACCA	TTTTTGGCTAAACGCTTTCAT
SASP	*Cxcl12*	GCCAACGTCAAGCATCTGAAA	CAGCCGTGCAACAATCTGAA
SASP	*Cxcl15*	TCCATGGGTGAAGGCTACTGT	TTCATTGCCGGTGGAAATTC
SASP	*Cxcl16*	GCACCCCTGCACATAGTCAGA	AGGACAGTGCTCCTGATGGAA
SASP	*Cxcl2*	TCAAGGGCGGTCAAAAAGTT	CAGTTAGCCTTGCCTTTGTTCA
SASP	*Fas*	CTGCACCCTGACCCAGAATAC	ACAGCCAGGAGAATCGCAGTA
SASP	*Fasl*	CCGCTCTGATCTCTGGAGTGA	CACGAAGTACAACCCAGTTTCG
SASP	*Foxo4*	CCACGAAGCAGTTCAAATGCT	TTCAGACTCCGGCCTCATTG
SASP	*GAPDH*	GACCTGACCTGCCGTCTAGAAA	CCTGCTTCACCACCTTCTTGA
SASP	*Gas6*	AGGCTCAACTACACCCGAACA	TTTAACTTCCCAGGTGGTTTCC
SASP	*Gata4*	GCTCCTACTCCAGCCCCTAC	CAGGACTGGGCTGTCGAA
SASP	*Gdf15*	TGTGCAGGCAACTCTTGAAGA	GCGATACAGGTGGGGACACT
SASP	*Hmgb1*	TCCTTCGGCCTTCTTCTTGTT	AGGATGCTCGCCTTTGATTTT
SASP	*Icam1*	GTGGCGGGAAAGTTCCTGTT	GTCCAGCCGAGGACCATACA
SASP	*Ifng*	TTGGCTTTGCAGCTCTTCCT	ATGACTGTGCCGTGGCAGTA
SASP	*Igf1*	AAAAGCAGCCCGCTCTATCC	CTTCTGAGTCTTGGGCATGTCA
SASP	*Igfbp2*	GCCCCCTGGAACATCTCTACT	GTTGTACCGGCCATGCTTGT
SASP	*Igfbp3*	ACCTGCTCCAGGAAACATCAGT	TTTCCACACTCCCAGCATTG
SASP	*Igfbp4*	GCAACTTCCACCCCAAACAGT	CCTGTCTTCCGATCCACACA
SASP	*Il10*	TGGCTCAGCACTGCTATGCT	TGTACTGGCCCCTGCTGATC
SASP	*Il12a*	ATCCTGCTTCACGCCTTCAG	GATAGCCCATCACCCTGTTGA
SASP	*Il12b*	GCCAGTACACCTGCCACAAAG	TGTGGAGCAGCAGATGTGAGT
SASP	*Il15*	GGCATTCATGTCTTCATTTTGG	TCCAGTTGGCCTCTGTTTTAGG
SASP	*Il17a*	GGACTCTCCACCGCAATGAA	GCACTGAGCTTCCCAGATCAC
SASP	*Il1a*	AAGAGACCATCCAACCCAGATC	CCTGACGAGCTTCATCAGTTTG
SASP	*Il1b*	TCAGGCAGGCAGTATCACTCA	CACGGGAAAGACACAGGTAGCT
SASP	*Il3*	GCCTGCCTACATCTGCGAAT	CGAAAGTCATCCAGATCTCGAA
SASP	*Il4*	TCCTCACAGCAACGAAGAACAC	AAGCACCTTGGAAGCCCTACA
SASP	*Il6*	ACCACGGCCTTCCCTACTTC	TTGGGAGTGGTATCCTCTGTGA
SASP	*Il8*	TCCATGGGTGAAGGCTACTGT	TTCATTGCCGGTGGAAATTC
SASP	*Inhba*	CAGGAAGACACTGCACTTTGA	TTCAGGAAGAGCCACACTTCT
SASP	*Irf1*	CAGCCGAGACACTAAGAGCAAA	GAGAAAGTGTCCGGGCTAACAT
SASP	*Lif*	GCTGTATCGGATGGTCGCATA	TCTGGTCCCGGGTGATATTG
SASP	*Mif*	GCCACCATGCCTATGTTCATC	GGGTGAGCTCCGACAGAAAC
SASP	*Mmp12*	GTGCCCGATGTACAGCATCTT	GGTACCGCTTCATCCATCTTG

bioRxiv preprint doi: https://doi.org/10.1101/2021.05.18.444618; this version posted May 19, 2021. The copyright holder for this preprint (which was not certified by peer review) is the author/funder, who has granted bioRxiv a license to display the preprint in perpetuity. It is made available under aCC-BY 4.0 International license.

SASP	*Mmp13*	TGAGGAAGACCTTGTGTTTGCA	GCAAGAGTCGCAGGATGGTAGT
SASP	*Mmp2*	TGTGGGTGGAAATTCAGAAGGT	ACTTGTTGCCCAGGAAAGTGA
SASP	*Mmp7*	TTGCTGCCACCCATGAATTT	TCACAGTACCGGGAACAGAAGA
SASP	*Mmp8*	TGGCTGCTCATGAATTTGGA	CATCAAGGCACCAGGATCAGT
SASP	*Mmp9*	TGAGTCCGGCAGACAATCCT	CCCTGGATCTCAGCAATAGCA
SASP	*Nfkb1*	GGCTTTGCAAACCTGGGAAT	TCCGTGCTTCCAGTGTTTCA
SASP	*Pappa*	CATCTCAGGTGTGTCGAACCA	TGCAAGGATACCAAGCATGCT
SASP	*Pdgfa*	CTCGAAGTCAGATCCACAGCAT	CAGCCCCTACGGAGTCTATCTC
SASP	*Pdgfb*	GCTGAGCTGGACTTGAACATGA	CCTCGAGATGAGCTTTCCAACT
SASP	*Serpinb2*	TTCCGCATACTGGAAACATCAG	GGATGCGTCCTCAATCTCATC
SASP	*Serpine1*	GGACACCCTCAGCATGTTCA	CGGAGAGGTGCACATCTTTCT
SASP	*Sparc*	GAGGAGGTGGTGGCTGACAA	CACCTTGCCATGTTTGCAAT
SASP	*Spp1*	GAGGAGGTGGTGGCTGACAA	CACCTTGCCATGTTTGCAAT
SASP	*Tgfb1*	AGCGCTCACTGCTCTTGTGA	GCTGATCCCGTTGATTTCCA
SASP	*Tgfb2*	GGTGGCGCTCAGTCTGTCTAC	TCTTGCGCATAAACTGATCCAT
SASP	*Tgfb3*	CTGTCCACTTGCACCACGTT	CCTAATGGCTTCCACCCTCTT
SASP	*Tgfbr1*	CGTGTGCCAAATGAAGAGGAT	AAGGTGGTGCCCTCTGAAATG
SASP	*Tnf*	GTTCTGCAAAGGGAGAGTGG	GCACCTCAGGGAAGAGTCTG
SASP	*Tnfrsf11b*	CCAAGAGCCCAGTGTTTCTT	CCAAGCCAGCCATTGTTAAT
SASP	*Tnfrsf12a*	CCGCCGGAGAGAAAAGTTTAC	GGGTGCTCCTCACTGGATCA
SASP	*Tnfsf10*	CTCTCGGAAAGGGCATTCATT	TCGATGACCAGCTCTCCATTC
SASP	*Tnfsf11*	GCTGGGACCTGCAAATAAGT	TTGCACAGAAAACATTACACCTG
SASP	*Vcam1*	GGCTCCAGACATTTACCCAGTT	CATGAGCTGGTCACCCTTGAA
SASP	*Vegfa*	GTACCTCCACCATGCCAAGTG	TGGGACTTCTGCTCTCCTTCTG

943